Measurement of K_S^0 Production and Collectivity in High Energy Nuclear Collision at RHIC

by

Zhaozhong Shi

Undergraduate Honors Thesis

Submitted for the degree of

Bachelor of Arts

in

Department of Physics

University of California, Berkeley

Approved

by

Faculty Advisor Date

Research Advisor Date

Abstract

The Solenoidal Tracker at Relativistic Heavy-Ion Collider (STAR) Collaboration collects and analyzes experimental data from the Relativistic Heavy-Ion Collider at Brookhaven National Laboratory. The STAR detector consists of the Time Projection Chamber (TPC), the Time of Flight (TOF) Detector, and the Heavy Flavor Tracker (HFT). The STAR detector covers full azimuthal angle at mid-rapidity with excellent particle identification. In 2014, STAR Collaboration implemented the HFT detector. The HFT detector enables precision determination of event and decay vertices. The main goal of the HFT detector is to perform precision measurement of the production of charm hadron in high energy nuclear collisions. In the meantime, it also allows clean measurements of proton. The Bachelors of Arts candidate carries out research at RNC Soft Physics Group at Lawrence Berkeley National Laboratory. The author uses event plane method to calculate the coefficient of second Fourier harmonic in the azimuth of K_S^0 particles using the data from 2014 for Au + Au at center of mass energy $\sqrt{s_{NN}}$ = 200GeV in STAR Collaboration. In addition, the author studies the number-of-quark scaling law from quark coalescence model for K_S^0 elliptic flow and confirms that K_S^0 is indeed created from quark-gluon plasma. The physics motivations and detail analyses will be presented in this thesis.

Table of Contents

Chapter 1 Introduction (Heavy-Ion Physics)

1.1 Review of Quantum Chromodynamics and High Energy Nuclear Physics

QCD as a Quantum Field Theory for Quarks and Gluons

Quantum Chromodynamics (QCD) is the quantum field theory of the strong interaction, a fundamental force describing the interactions between quarks and gluons, as the building blocks of hadrons. It is a non-abelian gauge field theory with SU(3) symmetry. The QCD Lagrangian is given by [1]

$$\mathcal{L}(\Psi, \bar{\Psi}) = \sum_{j} \bar{\Psi}_j [\gamma^{\mu}(i\partial_{\mu} - g_s t^a A^{\mu}_a) - m_j]\Psi_j - \frac{1}{4}G^a_{\mu\nu}G^{\mu\nu}_a \tag{1}$$

$t^a = \frac{\lambda^a}{2}$ is a possible set of linearly independent generators for SU(3). λ^a are the Gell-Mann Matrices. $G^a_{\mu\nu}$ is called the gluon-field tensor. It is defined by $G^a_{\mu\nu} = \partial_{\mu}A^a_{\nu} - \partial_{\nu}A^a_{\mu} + g f_{abc}A^b_{\mu}A^c_{\nu}$. f^{abc} are the structure constants for SU(3) such that $[T_a, T_b] = \sum f^{abc}T_c$. The values of a, b, and c are from 1 to 8. This Lagrangian density is invariant under SU(3) transformation of colors.

In the past 50 years, with the tremendous success of quantum electrodynamics (QED) and experiments from particle colliders, QCD, which shares similar features with QED, has also been well developed. It successfully explained and predicted the cross-section of particle productions in particle colliders and the decay lifetime for the decay process $\Delta^+ \rightarrow p + \pi^0$, which is determined by the strong coupling constant. Strong coupling constant as a function of momentum transfer is given by renormalization group theory [2]

$$\alpha_s(|q|^2) = \frac{12\pi}{(11N_c - 2N_f)\ln\left(\frac{|q|^2c^2}{\Lambda^2_{QCD}}\right)} \tag{2}$$

Here, N_f is the number of active quark flavors. $N_c = 3$ is the number of color. $q = k' - k$ is the four-momentum transfer of two particles. 100MeV$<\Lambda_{QCD}<$ 500MeV is called the QCD scale. Equation (2) is valid as long as $|q|^2c^2 >> \Lambda^2_C$.

Feynman Diagrams

Feynman diagrams is a useful tool to compute the interactions among particles. If we follow the Feynman Rules [2], we can compute the scattering amplitudes of these diagrams. Then, in QED, we will find that the scattering amplitudes of these diagrams can be expressed in the power of the coupling constant α because $\alpha = \frac{e^2}{4\pi\epsilon_0\hbar c} \approx \frac{1}{137}$. Here, ϵ_0 is the vacuum permittivity.

Perturbative QCD

According to Equation (2), for very large momentum transfer ($|p|^2c^2 >> \Lambda_{QCD}$), the strong coupling constant is very small. The strong interactions among particles can be studied from Feynman diagrams. The results can be expanded as the polynomials of α_s. When α_s is very small, the polynomial expansions converge. This version of QCD is called perturbative QCD. We can use perturbative QCD to study the early stage of high energy particle collisions with very large momentum transfers (The positive four-momentum transfer Q^2 is defined by $Q^2 = -q^2 > 0$). High energy physicists call this hard scattering process.

Non-perturbative QCD

Because the strong coupling constant increases as the momentum transfer decreases, when the momentum transfer is below the cutoff energy $\Lambda_{QCD} \approx 217$MeV, the strong coupling constant will be greater than 1. In this case, QCD is not perturbative. Quarks and gluons will be bounded by strong force and form hadrons such as baryons, which contain three quarks and mesons, which are the bound state of one quark and one antiquark. Physicists developed lattice gauge theory (lattice QCD) to perform numerical calculations to solve problems in non-perturbative region.

Asymptotic Freedom and Quark-Gluon Plasma

Unlike QED, the QCD coupling constant approaches zero as the energy increases or distance decreases due to the anti-screening effects of virtual gluons. This unique feature of QCD is called asymptotic freedom [3]. Therefore, in high energy nuclear collisions, quarks and gluons inside nuclei have high enough energy to overcome the Coulomb repulsion and get close enough to each other. They may be free from color confinement. Because heavy-ions such as gold, uranium, and lead contain many nucleons, when the impact parameter is small, many partons will participate in the reaction. Therefore, the multiplicity of quarks and gluons participating in the reaction is usually large. Normally, the multiplicity of partons is in the order magnitude of 10^3. The free quarks and gluons exist about 10^{-23}s and then form hadrons. When quarks and gluons reach local thermal equilibrium right after of heavy-ion collisions [4] the temperature of quarks and gluons are in the order magnitude of 10^{12}K. This hot and dense matter satisfies the criteria for plasma [5] because the Debye length is $\lambda_D = \frac{\hbar c}{g_s k_B T} \approx 0.4$fm [6]. The Debye length is much less than the size Time Projection Chamber, which is about 4.2m long [7]. Thus, it should demonstrate collective behavior. This system of quarks and gluons, which has color degree of freedom and collective behavior, is call quark-gluon plasma. In cosmology, it is believed that in the quark epoch, about 10^{-12}s to 10^{-6}s after the Big Bang, the universe was filled with leptons, photons, and quark-gluon plasma [8]. Nuclear and particle physicists would like to investigate the interactions of quarks and gluons from experiments and compare to the predictions of QCD.

Hadronic Gas

Similar to electrically charged neutral atom, when the temperature of quark-gluon plasma cools down, quarks and gluons will recombine and form color neutral hadrons. The interactions between hadrons by exchanging mesons are much weaker than the interactions between quarks and gluons. The interaction of hadron can be approximately described by Yukawa potential (screened Coulomb potential) $V(r) = \frac{k}{r} e^{-\frac{r}{r_0}}$ in non-relativistic limit. r_0 sets the scale of the interaction range between two hadrons. Therefore, when the distance between two hadrons is larger than r_0, the interaction strength of two hadrons is negligible. In this stage, the system of hadrons is called hadronic gas. Their dynamics can be described by the relativistic transport model.

QCD matters and QCD Phase Diagram

Our everyday atomic and molecular matters, which are bounded by electromagnetic interaction, has gas, liquid, and solid states. Similar to everyday matters, QCD matters, which are formed by strong interactions, also have different states. As I mention above, quark-gluon plasma and hadronic gas are good examples of QCD matters. There are other QCD matters such as the neutron stars and color superconducting state. The properties of QCD matters in different states are determined by their equations of state.

Similar to atomic matter, we use QCD phase diagram, shown in Figure 1, to describe different states of QCD matter. The horizontal axis of the diagram is the baryon chemical potential μ_B and the vertical axis is temperature T. The QCD phase diagram for different QCD matters is presented below

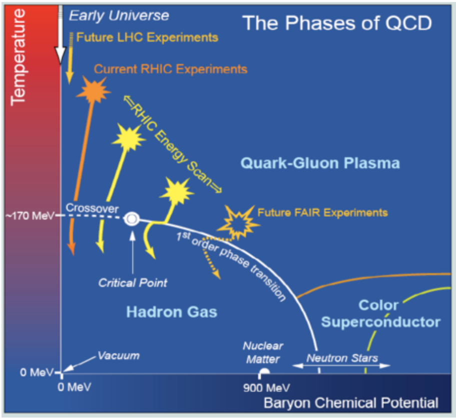

Fig. 1 The theoretical QCD phase diagram and the states of quark-gluon plasma, hadronic gas, neutron star, and color superconductor are shown as above. The solid line indicates the conjecture of first order phase transition between quark-gluon plasma and hadronic gas while the dash line is a smooth crossover. Image from [9].

Phase Transition

Lattice QCD calculations have predicted that the phase transition between quark-gluon plasma and hadronic gas is a smooth crossover near $\mu_B = 0$ [4]. At higher baryon chemical potential, theoretical calculations predict that the phase transition between quark-gluon plasma and hadronic gas is a first order phase transition [10]. The chiral symmetry restores in quark-gluon plasma phase while breaks in hadronic gas [4].

Critical Point

If the theoretical predictions are correct, according to thermodynamics, a critical point must exist between the first order phase transition and the smooth crossover. The theoretical calculations predict that the critical point is $\mu_B = 350 - 700\text{MeV}$ and $T_c \approx 160\text{MeV}$ [11].

Experimentally, the scale of the critical temperature may occur at $T_c \approx 175\text{MeV}$ [12] from high moment analyses. The research on critical point, a landmark in the QCD phase diagram, and the phase transition between quark-gluon plasma and hadronic gas are very important topics for physicists to understand the nature of QCD matters.

1.2 Relativistic Heavy-Ion Collisions

Motivations of Heavy-Ion Physics

High energy nuclear physicists focus on studying the interactions between quarks and gluons to decipher the structures and properties of hot and dense matter, known as quark-gluon plasma, which is formed right after of relativistic heavy-ion collisions. We accelerate heavy-ion, such as gold, uranium, and lead that contains many nucleons, to very high energy, in the order of GeV, and let them collide in order to create quark-gluon plasma. Because the speeds of the nuclei are near the speed of light, high energy nuclear collisions are relativistic. Because many nucleons participate in the reactions, the total number of particles created in relativistic heavy-ion collisions are larger than proton-proton collisions at the same energy. After the collisions, quark-gluon plasma may be created if the energy of the collisions is sufficiently high. Then, it expands due to the pressure gradient and cools down due to energy loss from gluon radiation. Quarks and gluons recombine and begin to form hadrons. The multiplicity of charged hadrons is in the order of 10^2 for each Au + Au collisions at 200GeV events. High energy physicists record the information of charged hadrons in relativistic heavy-ion collisions and analyze physical observables to understand quark-gluon plasma and decipher the structure of QCD phase diagram. Figure 2 shows the cartoon of heavy-ion collisions.

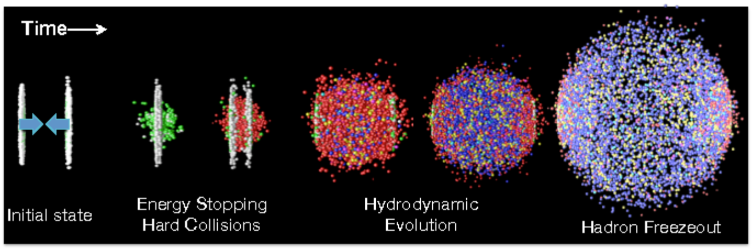

Fig. 2 An event in a typical heavy-ion collisions experiment is shown in Figure 2. It consists of four stages: initial state before the collision, the creation of quark-gluon plasma right after of the collision, hadronization after quark-gluon plasma expands and cools down, and the freeze-out stage when the inelastic scattering process ceases. Image from [13].

Heavy-Ion Collision Accelerators

Experimentally, to verify the theoretical predictions and study QCD matters created in extreme conditions, high energy nuclear physicists build high energy accelerators to accelerate heavy-ions such as gold, uranium, and lead to the energy that is high enough to break their nucleons and free quarks and gluons. Today, The Relativistic Heavy-Ion Collider (RHIC) at Brookhaven National Laboratory (BNL) and The Large Hadron Collider at the European Organization for Nuclear Research (CERN) are the two main accelerators for high energy nuclear collisions. The range of center-of-mass energy at RHIC is from 7.7GeV to 200GeV. The center-of-mass energy at LHC is about 2.76 - 5.5TeV. With a wide range of energy for heavy-ion collisions, high energy nuclear physicist can study the properties of QCD matters, verify the predictions of different theoretical models, and may discover new physics.

1.3 The Dynamics in Relativistic Heavy-Ion Collisions

The Conserved Quantities in Quark-Gluon Plasma

Because quark-gluon plasma has color degree of freedom, is color quasi-neutral, and the Debye length $\lambda_D << L$, it satisfy the criteria to be a plasma [5] and should demonstrate collective behaviors. Since strong interaction dominates in quark-gluon plasma, the net baryon number and strangeness are conserved. In addition, the electric charge, energy, and momentum are also conserved in heavy-ion collisions. Once quark-gluon plasma reaches thermal equilibrium, the state of the fluid may then be specified completely in terms of the local particle density and the local velocity [5]. Both of them are written into functions of space and time. The density is given by $n = n(x,t)$ and the four velocity is given by $u^\mu = u^\mu(x,t)$. Therefore, we can write down the continuity equation with conserved quantitates for quark-gluon plasma and use hydrodynamics to describe quark-gluon plasma.

Hydrodynamics Equations for Quark-Gluon Plasma

The hydrodynamics equations [14] of Quark-Gluon Plasma consist of three parts: the equation of motion from conservation of energy and momentum, the continuity equation from conserved currents, and the equation of state of quark-gluon plasma near zero chemical potential.

a. The Equation of Motion

$$\partial_\mu T^{\mu\nu} = 0 \tag{3}$$

Here, $T^{\mu\nu}$ is the energy-momentum tensor. It is defined by [14]

$$T^{\mu\nu} = (\epsilon + P)u^\mu u^\nu - P g^{\mu\nu} \tag{4}$$

Equation (3) is the local conservation of energy. P is the pressure and ϵ is the energy density. They are determined by the equation of state.

b. The Continuity Equation

$$\partial_\mu J_i^\mu = 0 \tag{5}$$

Here, J_i^μ is the conserved current. Equation (5) is the local conservation of current. To investigate the bulk properties of quark-gluon plasma, we only consider net baryon current in our hydrodynamics equations. The relativistic net baryon current is given by

$$J_B^\mu = n_B u_B^\mu \tag{6}$$

Here, n_B is the baryon number density and u^μ is its four velocity. In addition, the conservation of current equation is Lorentz invariant.

c. Equation of States of Quark-Gluon Plasma

According to the MIT Bag Model [15], the equation of state of quark-gluon plasma at zero quark chemical potential $\mu_q = 0$ with zero quark mass $m_q = 0$ approximation in thermal equilibrium is given by [4]

$$P = [2(N_c^2 - 1) + \frac{7}{2}N_f N_c]\frac{\pi^4 k^4}{90\hbar^3 c^3}T^4 - B \tag{7}$$

$$\epsilon = [2(N_c^2 - 1) + \frac{7}{2}N_f N_c]\frac{\pi^4 k^4}{30\hbar^3 c^3}T^4 + B \tag{8}$$

In Equation (7) and (8), N_f is the number of flavor and N_c is the color degree of freedom. The bag constant is given by $B \approx 200\mathrm{MeV/fm}^3$. Here, for quark-gluon plasma, $N_c = 3$ for SU(3) strong interaction. We should note that quantum effects are only taken into account in the equation of state of quark-gluon plasma. We can solve the hydrodynamics equations from Equation (2) - (8) to theoretically study the bulk properties of quark-gluon plasma.

1.4 General Formulations for High Energy Physics Experiments

Relativistic Kinematics

In high energy physics experiments, the speed of particles are almost speed of light. Therefore, we need to apply relativistic kinematics to understand the physics from the experiments. In the rest frame, the momentum and energy of a free particle of mass m and velocity $\mathbf{v}$ are given by

$$\mathbf{p} = \frac{m\mathbf{v}}{\sqrt{1-\frac{v^2}{c^2}}} = \gamma\beta mc \tag{9}$$

$$E = \sqrt{\mathbf{p}^2c^2 + m^2c^4} = \gamma mc^2 \tag{10}$$

Where $\beta = \frac{v}{c}$ and $\gamma = \frac{1}{\sqrt{1-\frac{v^2}{c^2}}} = \frac{1}{\sqrt{1-\beta^2}}$

Lorentz Transformation

Let the coordinate of a reference frame A to be (t, x, y, z) and the other reference frame B to be (t', x', y', z') moving relative to A with velocity v in the x-axis. We have [16]

$$\begin{bmatrix} t' \\ x' \\ y' \\ z' \end{bmatrix} = \begin{bmatrix} \gamma & \gamma\beta & 0 & 0 \\ \gamma\beta & \gamma & 0 & 0 \\ 0 & 0 & 1 & 0 \\ 0 & 0 & 0 & 1 \end{bmatrix} \begin{bmatrix} t \\ x \\ y \\ z \end{bmatrix} \tag{11}$$

The equation above is called the Lorentz Transformation. It is a orthogonal transformation.

Energy in the Center of Mass Frame

The Lorentz invariant variable s is defined [2]

$$s = (p_1 + p_2)^2c^2 = (p_1^2 + p_2^2 + 2p_1p_2)c^2 \tag{12}$$

Here $p_1 = (\frac{E_1}{c}, \mathbf{p_1})$ and $p_2 = (\frac{E_2}{c}, \mathbf{p_2})$ are four-momenta.

In the center of mass frame, because $\mathbf{p_1} + \mathbf{p_2} = 0$, we have

$$s = (E_1 + E_2)^2 = E_{CM}^2 \tag{13}$$

Therefore

$$E_{CM} = \sqrt{s} \tag{14}$$

In this thesis, the gold and gold nuclei collisions are at center of mass energy $\sqrt{s_{NN}} = 200\text{GeV}$. According to Equation (13), the energy of each gold nucleus is 100GeV in the center of mass frame.

Momentum Coordinate in High Energy Physics Experiments

Non-relativistically, the momentum space has a Cartesian coordinate (p_x, p_y, p_z). Figure 3 shows the definitions of Cartesian coordinates and spherical coordinates.

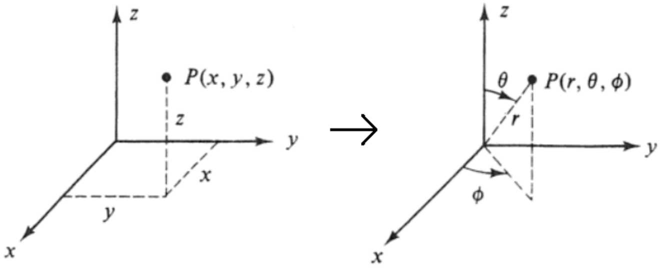

Fig. 3 The definitions of Cartesian coordinates (x, y, z) and spherical coordinates (r, θ, ϕ) are shown above. Image from [17].

In experimental high energy physics, we use different coordinates. We define rapidity y as follows

$$y = \frac{1}{2}\ln\left(\frac{E + p_z c}{E - p_z c}\right) \tag{15}$$

Here, the energy is $E = \sqrt{p_x^2 c^2 + p_y^2 c^2 + p_z^2 c^2 + m^2 c^4}$ according to Equation (10).

The transverse momentum p_T

$$p_T = \sqrt{p_x^2 + p_y^2} \tag{16}$$

The azimuthal angle ϕ

$$\phi = \arctan\left(\frac{p_y}{p_x}\right) \tag{17}$$

The pseudo-rapidity η

$$\eta = -\ln[\tan\left(\frac{\theta}{2}\right)] \tag{18}$$

Here, the angle $\theta = \arccos\left(\frac{p_z}{\sqrt{p_x^2+p_y^2+p_z^2}}\right)$ is defined by the spherical coordinate in Figure 3.

Therefore, we can transform (p_x, p_y, p_z) to (p_T, ϕ , y) according to Equation (15) to (17). We should note that the p_T and ϕ are Lorentz invariant because they are perpendicular to the Lorentz boost direction (z-direction).

1.5 Bulk Medium Properties in Relativistic Heavy-Ion Collision Experiments

Hadron Spectrum

The hadrons form when quark-gluon plasma cools down. Since quark-gluon plasma reaches local thermal equilibrium, the hadronic gas should obey the relativistic Boltzmann distribution

$$\frac{d^6N(x,y,z,p_x,p_y,p_z)}{dxdydzdp_xdp_ydp_z} \propto e^{-\frac{E}{kT}} \tag{19}$$

Experimentally, we care about the momentum distribution of particles. Therefore, we would like to study the distribution function in (p_T, ϕ, y) coordinates so that the transverse momentum distribution is Lorentz invariant for a given rapidity range.

$$\frac{d^3N(p_T,y,\phi)}{p_Tdp_Tdyd\phi} = \frac{d^2N_1(p_T,y)}{p_Tdp_Tdy}\frac{dN_2(\phi)}{d\phi} \tag{20}$$

We should note that $N(p_T,y,\phi) = N_1(p_T,y)N_2(\phi)$ is separable in the (p_T, ϕ, y) coordinates. In this thesis, I will focus on studying the distribution function $\frac{dN_2(\phi)}{d\phi}$ in the next sections.

Collective Flow in Heavy-Ion Collisions

In high energy nuclear collisions, we assume partons reach local thermal equilibrium right after of collisions [4]. In addition, the pressure gradient among constituents push quarks and gluons outwards and make quark-gluon plasma expand. All particles tend to move away from the collision center. Therefore, the total velocities of particles consist of two components: the random component due to thermalization and the radially outward component due to pressure gradient. The emission of particles with collective behavior is called the collective flow. Collective flow includes longitudinal flow and transverse flow.

Azimuthal Anisotropy in Relativistic Heavy-Ion Collisions

As we know, the impact parameter in heavy-ion collision is generally not zero. Therefore, the overlapping region where quarks and gluons interact, is an almond shape, which is not radially symmetric. Therefore, after nuclei collide, the emissions of particles are not uniform for all azimuthal angles. The azimuthal angular dependence of the particles emissions in heavy-ion collisions is called the azimuthal anisotropy. Since we know that the range of ϕ is from 0 to 2π, mathematically, we can use Fourier series to describe the azimuthal anisotropy in heavy-ion collisions.

Event Plane Formulation for Flow Analysis

a. Creation of Coordinates

Voloshin and Zhang [18] suggest to use a Cartesian coordinate to describe the motions of two nuclei beams in heavy-ion collisions. We let the z-direction (longitudinal) to be the beam direction and the x direction to be the direction of the impact parameter. According to right hand rule, we can immediately get the y-direction. According to Figure 3, we can identify the angle θ and ϕ for the corresponding spherical coordinate. The Cartesian coordinate for heavy-ion collisions is shown as below in Figure 4

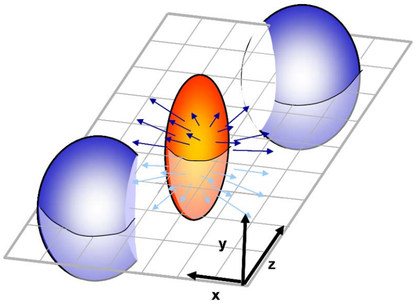

Fig. 4 The figure above shows the ellipsoid of the overlapping region of two nuclei in heavy-ion collisions. The event plane, which is the x-z plane shown as above, is constructed by the beam direction and the impact parameter vector. The emissions of particles are anisotropic in the x-y plane. Image from [19].

Then we use the event plane (the x-z plane), which is determined by the beam direction and the direction of impact parameter, to analyze the emissions of particles. The geometric shape in the x-y (transverse direction) plane is ϕ dependent. This geometric asymmetry, shown in Figure 5, leads to the anisotropy of pressure gradient. The semi-minor axis has the greatest pressure gradient and the semi-major axis has the smallest pressure gradient.

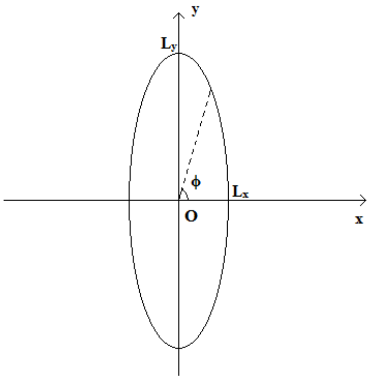

Fig. 5 The ellipse shown in Figure 5 is the projection of the almond shape of the reaction region on the x-y axis. The semi-major axis is the L_y and semi-minor axis is L_x. We expect the emission to be anisotropic because the pressure gradient is greater in the x-axis than the y-axis. Image from the author in this thesis.

b. Transverse Flow and Longitudinal Flow

As we can see, the anisotropic pressure gradient exists in the x-y plane. The transverse emissions of particles is anisotropic. The collective motion particles in the transverse direction is called transverse flow. Similarly, the collective motion of particles in the longitudinal (beam) direction (z-axis) is called the longitudinal flow. Most detectors can cover a large solid angle in the transverse direction and measure the momentum and energy of the particles. For instance, the STAR experiment and the CMS experiment have full azimuthal angle coverage [7, 20]. Therefore, we focus on analyzing and studying the transverse flow in relativistic heavy-ion collisions.

c. Anisotropic Pressure in the Reaction Region

Classically, according to Newton's Second Law, we know that

$$\nabla \cdot \mathbf{P} = \rho(r)a \tag{21}$$

Hence,

$$\mathbf{p} = m\int_0^\tau a dt = m\int_0^\tau \frac{\nabla \cdot \mathbf{P}}{\rho(r)} dt \approx m\tau\frac{\nabla \cdot \mathbf{P}}{\rho(r)} \tag{22}$$

$\rho(r)$ is the density of quark-gluon plasma, m is the mass of a particle, and τ is the existence time of quark-gluon plasma. The pressure here is a 3×3 symmetric tensor

$$P = \begin{bmatrix} P_{xx} & P_{xy} & P_{xz} \\ P_{yx} & P_{yy} & P_{yz} \\ P_{zx} & P_{zy} & P_{zz} \end{bmatrix}$$

If we assume there is no collisions in quark-gluon plasma, the shear viscosity is negligible. Therefore, the off-diagonal elements of the pressure tensor are zero. Thus, we have

$$P = \begin{bmatrix} P_x & 0 & 0 \\ 0 & P_y & 0 \\ 0 & 0 & P_z \end{bmatrix}$$

d. Fourier Analysis

We can approximate the pressure gradient by $\nabla \cdot \mathbf{P} \approx \frac{P_0}{r}$. As we can see, the distance r from the boundary to the origin is a function of ϕ. the pressure gradient is maximum in the semi-minor axis and minimum at the semi-major axis. Therefore, according to Equation (22), the transverse momentum p_T will depend on the azimuthal angle ϕ. Thus, for transverse flow, we can use Fourier series to parametrize the azimuthal distribution of particle emissions [18].

$$\frac{dN_2(\phi)}{d\phi} = \frac{x_0}{2\pi} + \sum_{n=1}^{\infty}[x_n(p_T)\cos(n\phi) + y_n(p_T)\sin(n\phi)] \tag{23}$$

According to trigonometry, we get

$$\frac{dN_2(\phi)}{d\phi} = \frac{x_0}{2\pi} + \sum_{n=1}^{\infty} 2v_n(p_T)\cos[n(\phi - \Psi_n)] \tag{24}$$

Here, $v_n = \frac{1}{2}\sqrt{x_n^2 + y_n^2}$ and $\Psi_n = \frac{1}{n}\arctan\left(\frac{y_n}{x_n}\right)$.

e. Recentering the Event Plane

Theoretically, we know that x_n and y_n are independent variables. The fraction $\frac{y_n}{x_n}$ can take any value with equal probability. Because $\Psi_n = \frac{1}{n}\arctan\left(\frac{y_n}{x_n}\right)$, the Ψ_n distribution should be completely random and independent of the events, it can take any value from 0 to π with equal probability. Hence, the Ψ_n distribution should be uniform. To estimate the event plane, we first arbitrarily choose an a coordinate and get a sinusoidal Ψ_n distribution. To make the distribution uniform, we need to do the following steps suggest by Poskanzer and Voloshin [21]

Step 1. Calculating the Track Level q Vector $\mathbf{q} = (q_x, q_y)$

$$q_x = \frac{1}{N_{tracks}} \sum_{i=1}^{N_{tracks}} \cos(n\phi) \tag{25}$$

$$q_y = \frac{1}{N_{tracks}} \sum_{i=1}^{N_{tracks}} \sin(n\phi) \tag{26}$$

Step 2. Calculating the Event Level Q Vector $\mathbf{Q} = (Q_x, Q_y)$

$$Q_x = \frac{1}{N_{events}} \sum_{j=1}^{N_{events}} q_x \tag{27}$$

$$Q_y = \frac{1}{N_{events}} \sum_{j=1}^{N_{events}} q_y \tag{28}$$

Step 3. Subtracting the Event Level Q Vector from all Tracks for Corrections

$$q_x^{Corrected} = \frac{1}{N_{tracks}} \sum_{i=1}^{N_{tracks}} [\cos(n\phi) - Q_x] \tag{29}$$

$$q_y^{Corrected} = \frac{1}{N_{events}} \sum_{i=1}^{N_{tracks}} [\sin(n\phi) - Q_y] \tag{30}$$

Step 4. Calculate of Ψ_n and $\Psi_n^{Corrected}$

$$\Psi_n = \frac{1}{n}\arctan\left(\frac{q_y}{q_x}\right) \tag{31}$$

$$\Psi_n^{Corrected} = \frac{1}{n}\arctan\left(\frac{q_y^{Corrected}}{q_x^{Corrected}}\right) \tag{32}$$

This process is called recentering. We expect the Ψ_n distribution to be sinusoidal and the $\Psi_n^{Corrected}$ distribution to be uniform.

We expect the angle Ψ_n distribution to be sinusoidal before recentering because the cross-section of the event plane with the almond shape reaction region is an ellipse. After recentering, we expect the $\Psi_n^{Corrected}$ distribution to be uniform (independent of ϕ) because the cross-section will become a circle.

f. Estimating the Event Plane Resolution

The event plane we reconstruct is certainly not a perfect estimate of the event plane in the experiment. There are statistical fluctuations in our estimate. The event plane we estimate will smear. In other words, the track level q vector for each event should obey the Gaussian distribution. The mean of the Gaussian is the corrected q vector [22]. To evaluate how well our event plane is reconstructed, we can calculate the event plane resolution using two equal amount of subevents and calculate their correlations. A typical way to do this is to separate the event plane into positive and negative pseudo-rapidities η and evaluate the angle Ψ_n as Ψ_n^a for $\eta > 0$ and Ψ_n^b for $\eta < 0$. The full event plane resolution R, ranged from 0 to 1, can be obtained by [18]

$$\sqrt{\langle \cos[n(\Psi_n^a - \Psi_n^b)] \rangle} = G(\chi_m) = \frac{\sqrt{\pi}}{2\sqrt{2}} \chi_m e^{\frac{-\chi_m^2}{4}} [I_{\frac{k-1}{2}}(\frac{-\chi_m^2}{4}) + I_{\frac{k+1}{2}}(\frac{-\chi_m^2}{4})] \tag{33}$$

Here, I_ν is the modified Bessel function of order ν. We can numerically solve χ_m from the equation above, multiply χ_m by $\sqrt{2}$, then substitute it back G. We will get the full event resolution R

$$R = G(\sqrt{2}\chi_m) = G[\sqrt{2}G^{-1}(\sqrt{\langle \cos[n(\Psi_n^a - \Psi_n^b)] \rangle})] \tag{34}$$

Anisotropic Flow

To find the Fourier coefficients v_n, we can apply the Fourier tricks to find x_n and y_n.

Theoretically, because the function $\frac{dN_2(\phi)}{d\phi}$ is continuously analytical, we can use integral to find the Fourier coefficients [18]

$$x_n = 2 \int_0^{2\pi} \frac{dN_2(\phi)}{d\phi} \cos(n\phi) d\phi \tag{35}$$

$$y_n = 2 \int_0^{2\pi} \frac{dN_2(\phi)}{d\phi} \sin(n\phi) d\phi \tag{36}$$

Experimentally, because our data are discrete values, we can convert the integral into a sum

$$x_n = \frac{2}{N} \sum_{n=1}^{N} \cos(n\phi) d\phi = 2\langle \cos n\phi \rangle \tag{37}$$

$$y_n = \frac{2}{N} \sum_{n=1}^{N} \sin(n\phi) d\phi = 2\langle \sin n\phi \rangle \tag{38}$$

Here, we sum up all tracks in the experiment to get the x_n and y_n. Then, we will be able to find

$$v_n = \frac{1}{2}\sqrt{x_n^2 + y_n^2} = \sqrt{(\langle\cos n\phi\rangle)^2 + (\langle\sin n\phi\rangle)^2}. \tag{39}$$

Directed Flow and Its Physics

By definition, the directed flow is the coefficient of the first Fourier harmonics in the momentum distribution of the particles created from high energy nuclear collisions

$$v_1 = \sqrt{(\langle\cos\phi\rangle)^2 + (\langle\sin\phi\rangle)^2} \tag{40}$$

It describes the magnitude of the total vector sum of transverse momenta. In the center of mass frame, we know that the total momentum $\mathbf{p} = 0$. Therefore, $\langle p_T \cos\phi\rangle = \langle p_T\rangle\langle\cos\phi\rangle = 0$ and $\langle p_T \sin\phi\rangle = \langle p_T\rangle\langle\sin\phi\rangle = 0$. Thus, because $\langle p_T\rangle > 0$, we have $\langle\cos\phi\rangle = \langle\sin\phi\rangle = 0$.

Elliptic Flow and Its Physics

By definition, the elliptic flow is the coefficient of the second Fourier harmonic in the azimuthal distribution of the particles created from relativistic heavy-ion collisions.

$$v_2 = \sqrt{(\langle\cos 2\phi\rangle)^2 + (\langle\sin 2\phi\rangle)^2} = \sqrt{(\langle\cos^2\phi - \sin^2\phi\rangle)^2 + (\langle 2\sin\phi\cos\phi\rangle)^2} \tag{41}$$

But since we have

$$\langle\cos\phi\rangle = \langle\sin\phi\rangle = 0 \tag{42}$$

$$v_2 = \sqrt{(\langle\cos^2\phi - \sin^2\phi\rangle)^2} = \langle\cos^2\phi - \sin^2\phi\rangle = \langle\frac{p_x^2 - p_y^2}{p_T^2}\rangle \tag{43}$$

Therefore, classically, because we already have

$$p_x \approx \frac{m\tau}{\rho(r)}\frac{\partial P}{\partial x} \approx \frac{m\tau}{\rho(r)}\frac{P}{L_x} \tag{44}$$

$$p_y \approx \frac{m\tau}{\rho(r)}\frac{P}{L_y} \tag{45}$$

$$p_T^2 = p_x^2 + p_y^2 \approx \frac{P^2\tau^2}{\rho(r)^2}(\frac{1}{L_x^2} + \frac{1}{L_y^2}) \tag{46}$$

Hence, substitutes these into the equation of v_2, we get

$$v_2 \approx \langle \frac{L_x^2 - L_y^2}{L_x^2 + L_y^2} \rangle \tag{47}$$

We define the eccentricity $\epsilon = \frac{L_x^2 - L_y^2}{L_x^2 + L_y^2}$. The elliptic flow v_2 mainly describes the average eccentricity of the almond shape of the overlapping region of two nuclei shown as Figure 5.

Therefore, classically, v_2 is roughly proportional to the eccentricity of the geometric shape. In fact [23],

$$v_2 = \epsilon f(n, R, p_T) \tag{48}$$

In addition, v_2 depends on the shear viscosity η_s and the bulk viscosity [24], which determine the off-diagonal elements of the pressure tensor, if we consider collisions in quark-gluon plasma. Theoretically, the elliptic flow v_2 can be parameterized by [25]

$$v_2 = v_2^{max} \tanh[\frac{p_T}{p_0(\chi)}] \tag{49}$$

χ is called the opacity. p_0 scales the saturation of v_2 in high p_T.

1.6 High Energy Nuclear Physics Experiments

Experiments at Relativistic Heavy Ion Collider in Brookhaven National Laboratory

a. STAR Experiment

The Solenoidial Tracker At Relativistic Heavy Ion Collider (STAR) Experiment analyzes experimental data from Relativistic Heavy Ion Collider (RHIC) at Brookhaven National Laboratory. STAR collaboration measures important quantities, analyzes experimental data, studies the properties of quark-gluon plasma, and understands the QCD phase diagram from RHIC. The experimental setup of STAR and a preview of experimental observations are shown as Figure 6 and Figure 7.

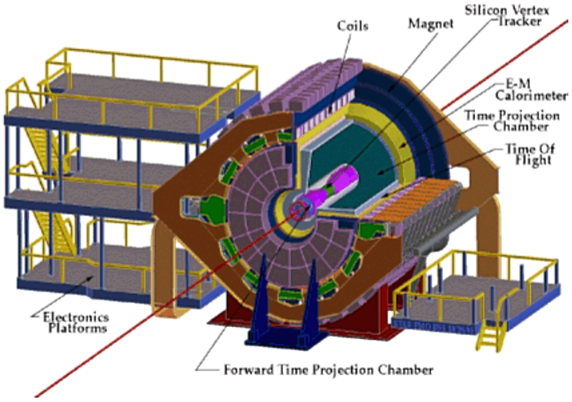

Fig. 6 The STAR experimental setup contains the Time Projection Chamber (TPC) to measure energy loss along with the Time of Flight (TOF) facility for particle identification, the E-M Calorimeter to detect and measure photon radiation in heavy-ion collisions, and the upgraded silicon Heavy-Flavor Tracker with 4 layers to measure charmed particles like D^0 mesons [26]. Image from [27].

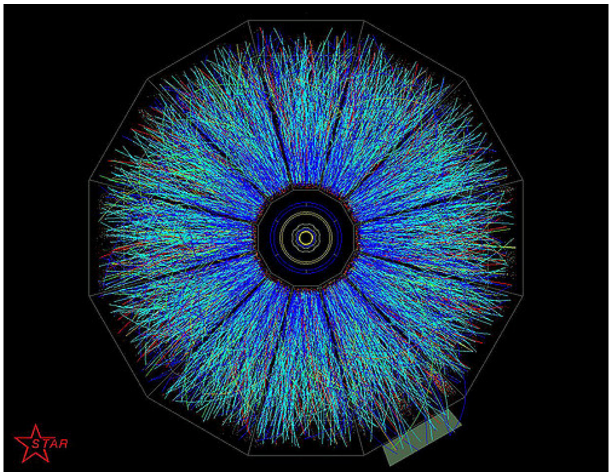

Fig. 7 A preview of the particles emissions from Au + Au collisions at 200GeV inside the Time Projection Chamber of STAR experiment is presented above. Image from [28]

The pseudo-rapidity coverage of STAR TPC is -1.8 $< \eta <$ 1.8 [7]. STAR collaboration plans to scan beam energies from 7.7 GeV to 200GeV to locate points on QCD phase diagram and understand its structure. The proposed Beam Energy Scan Program and the Fixed Target

Program from 2016 to 2021 will hopefully provide evidences for the phase transition between quark-gluon plasma and hadronic gas and find the critical point in QCD phase diagram.

b. PHENIX Experiment

In addition to studying the properties of quark-gluon plasma and the structure of QCD phase diagram, the PHENIX Experiment focuses on studying the spin structure of protons from polarized proton beams [29]. Figure 8 shows the experimental setup of PHENIX Experiment

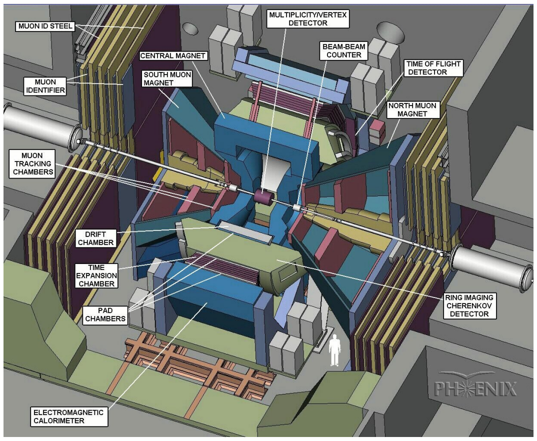

Fig. 8 The PHENIX detector is shown as above. Phenix detectors do not cover full azimuthal angles. Image from [30].

Experiments at Large Hadron Collider in European Organization for Nuclear Research

ALICE experiment

A Large Ion Collider Experiment (ALICE) at Large Hadron Collider (LHC) in European Organization for Nuclear Research (CERN) conducts research on heavy-ion collision experiments at higher beam energy. A typical heavy-ion collision experiment is Pb + Pb at $\sqrt{s_{NN}} = 2.76$TeV. ALICE experiment has scientific programs on transverse flow and jet quenching analyses to study the properties of quark-gluon plasma and the early stage of the universe [31]. ALICE experiment has the following experimental setup

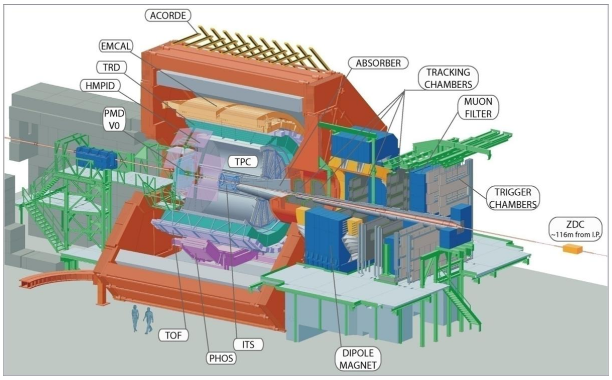

Fig. 9 The ALICE detector is shown as above. The pseudo-rapidity coverage of the ALICE TPC is -0.9 $< \eta <$ 0.9 for full radial track length [32]. It can detect a wider range of charged particle than PHENIX experiment. Image from [33].

CMS Experiment

The Compact Muon Solenoid (CMS) Experiment also analyzes heavy-ion collisions data from LHC [34]. It has high energy particle physics program and heavy-ion physics program. The CMS experiment analyzes p-p and Pb-Pb collisions. The structure of the CMS detector is shown in Figure 10.

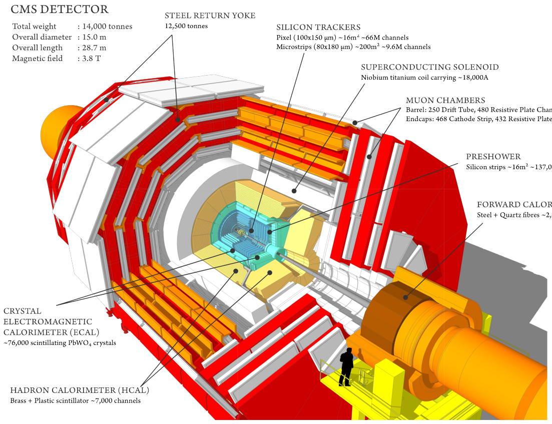

Fig. 10 The CMS detector is shown as above. It is an excellent detector for heavy-ion collisions experiments. The pseudo-rapidity coverage of the CMS Hadronic Calorimeter is -5.0 $< \eta <$ 5.0 and the tracker is about -2.4 $< \eta <$ 2.4 [20]. It can measure particles with transverse momentum with high resolution range from 0.25GeV/c to 100GeV/c. Image from [35].

ATLAS Experiment

The ATLAS Experiment also has heavy-ion physics program. ATLAS Collaborations studies elliptic flow, jet physics, and quarkonium production in Pb + Pb collisions at LHC [36]. The experimental setup for ATLAS Experiment is presented in Figure 11

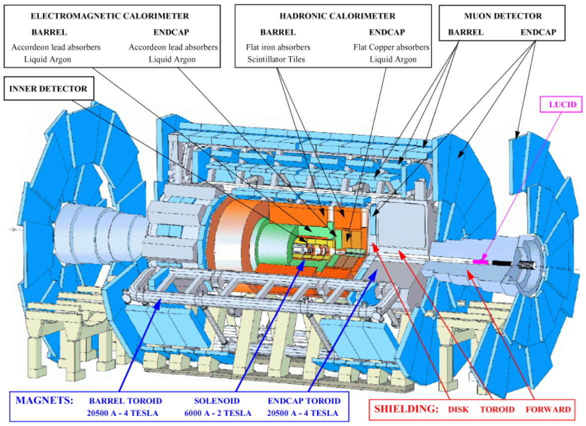

Fig. 11 The ATLAS detector is shown as above. It can measure elliptic flow and quarkonium production in Pb + Pb collisions. Image from [37].

Chapter 2 Analysis Details and Preliminary Results

2.1 STAR Instrumentations

a. Time Projection Chamber (TPC)

The Time Projection Chamber [7] serves as a primary tracking instrument in STAR experiment. The TPC records the helix tracks of electric charged particles, such as proton, pion, and kaon, measures the momenta of charged particle from the helix tracks, and measure the ionization energy loss (dE/dx) for particle indentification. It covers a pseudo-rapidity of -1.8 $< \eta <$ 1.8. The structure of TPC is shown as follows in Figure 12.

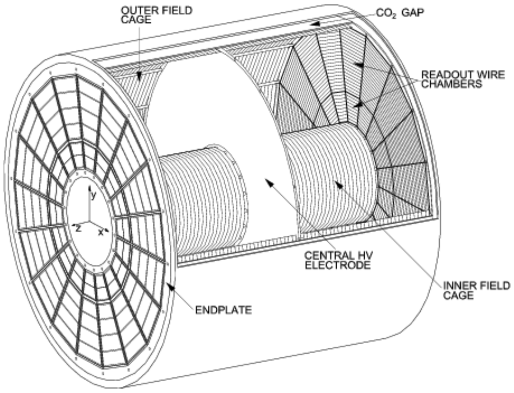

Fig. 12 The structure of TPC is shown above. It consists of inner field cage and outer field cage with CO_2 in between. Image from [38].

b. Time of Flight Device for Particle Identification (TOF)

The Time of Flight device is a barrel detector employing Multi-gap Resistive Plate Chamber Technology [39]. Along with the TPC, TOF can significantly reduce the integrated luminosity requirement for the elliptic flow of baryons containing multiple strange quarks such as Ω and Ξ. In addition, it can extend the p_T to about 1 to 2GeV/c for accurate measurement of velocity for particle identification (PID). PID performance for pion, kaon, and proton is shown in Figure 13.

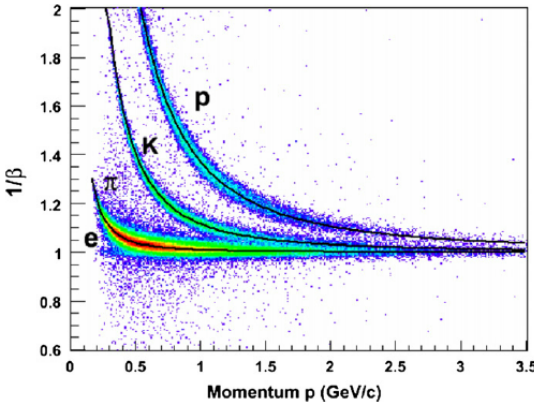

Fig. 13 The inverse velocity $1/\beta$ vs p_T for pion, kaon, proton with TOF is shown as above. TOF can expend the identification pion and kaon to approximately 3.0GeV/c with high accuracy according to Figure 13. Image from [40].

In this thesis, I use TPC along with TOF to identify pions up to 3.0GeV/c and analyze the elliptic flow of K_S^0.

c. The Heavy Flavor Tracker (HFT)

In Run 14, STAR Collaboration implemented the Heavy Flavor Tracker detector (HFT). HFT applies active pixel sensors and silicon strip technology [41]. Figure 14 shows the structure of HFT

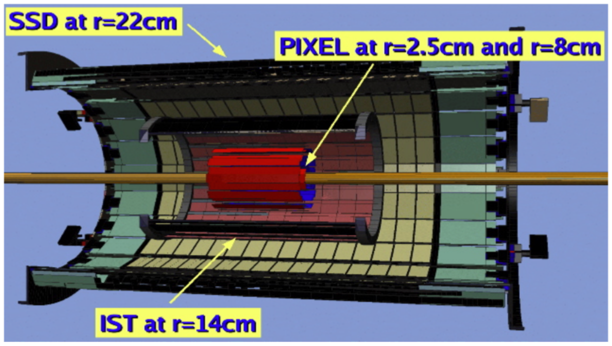

Fig. 14 The HFT consists of 4 layers of silicon detectors the Silicon Strip Detector (SSD), Intermediate Silicon Tracker (IST), the two-layer Silicon Pixel Detector (PIXEL). Image from [41].

With HFT, we can reconstruct K_S^0 particles in very low transverse momentum ($p_T = 50$MeV) and study its elliptic flow at very low p_T. The pointing resolution of HFT is shown as follows

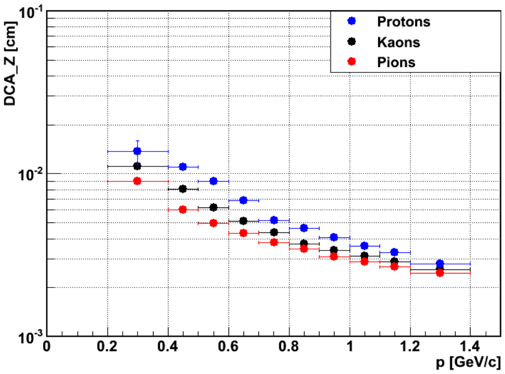

Fig. 15 The HFT point resolution is shown as above. The high resolutions at low transverse momentum (p_T <0.3GeV/c) enable us to precisely measure the low transverse momentum K_S^0 particles. Image from [42].

2.2 Analysis of Experimental Data

I. Preparations for K_S^0 Elliptic Flow Analysis for Run 14 Data with Heavy Flavor Tracker

1. Event Plane Method to Calculate Elliptic Flow

There are several methods such as the event plane method, two-particle correlations method, and four-particle correlation method [43] to calculate the elliptic flow. In this thesis, I use event plane method to calculate the K_S^0 elliptic flow. In addition, in order to diminish the non-flow effect of jets in our event plane reconstruction, I use the η subevent method [21]. In this method, I will subtract the $\eta > 0$ K_S^0 ϕ from the $\Psi_2^{Corrected}$ of $\eta < 0$ and the $\eta < 0$ K_S^0 ϕ from the $\Psi_2^{Corrected}$ of $\eta > 0$.

2. Decay Channel for K_S^0

In high energy nuclear collisions, K_S^0 is created from quark-gluon plasma and then decays. Most K_S^0 particles directly come from the hadronization of quark-gluon plasma and decay into pion pairs. A very little fraction of K_S^0 particles come from the charm decay of Λ_C^+. The Λ_C^+ decay channel is $\Lambda_C^+ \rightarrow p + K_S^0$ and then $K_S^0 \rightarrow \pi^+ + \pi^-$. I reconstruct K_S^0 from π^+ and π^- pairs. Because the lifetime of K_S^0 is 8.948×10^{-11}s, the decay length of K_S^0 is 2.6844cm [44]. Figure 16 shows K_S^0 decay

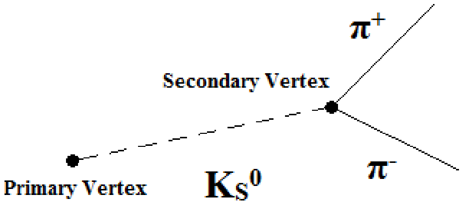

Fig. 16 The K_S^0 decay channel $K_S^0 \rightarrow \pi^+ + \pi^-$ is shown as above. Image from the author in this thesis.

In this thesis, the total number of Au + Au collisions events is about 466 million.

3. Track Selection

As we can see from Figure 7, a typical event has hundreds of tracks. In order to select high quality tracks for my analysis, I impose several cuts on the tracks. I require the TPC fit points to be greater than 20. Also, there are at least 1 hit per HFT layer. The distance of closest approach (DCA) from the tracks to the primary vertex where the K_S^0 is created is greater than 0.1cm.

4. Event Selection

The centrality is determined by the radius of the nucleus and the impact parameter. The larger the impact parameter is, the more peripheral the collision is. Experimentally, the centrality is extracted from the number of charged particles created in heavy-ion collisions and compared to Monte Carlo Glauber model calculations. The more particle are created, the more central the collisions is. STAR Collaboration measures centrality regions from 0 to 80%. In my analysis, the centrality is divided into 9 bins. 0 - 5%, 5 - 10%, 10 - 20%, 20 - 30%, 30 - 40%, 40 - 50%, 50 - 60%, 60 - 70%, and 70 - 80%. The elliptic flow of K^0_S vs p_T plots will be presented in these 9 bins.

5. Topological Cuts for K^0_S

To select pions pairs for K^0_S construction, I impose cuts on the tracks. The cut parameters are defined in Figure 17.

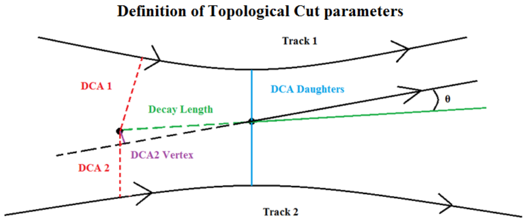

Fig. 17 Figure 17 defines the topological cuts parameters on pion candidates for K^0_S particle reconstruction. Image from the author in this thesis.

From Figure 17, we can see that the Decay Length, θ, and DCA2 Vertex satisfy the relations DCA2 Vertex = Decay Length$\times\sin\theta$. Therefore, there are five independent parameters for topological cuts. I choose DCA1, DCA2, DcaDaughters, θ, and DCA2 Vertex as my topological cuts parameters for pion pairs in my analysis. In addition, the HFT requires the Decay Length on the x-y plane to be less than 1.5cm [41]. The cuts I apply to select pion candidates for K^0_S reconstruction are shown in Table 1.

Topological Cut Parameters for K^0_S Reconstruction		
DCA1 $>$ 0.12cm	DCA2 $>$ 0.12cm	DcaDaughters $<$ 0.02
$\cos\theta > 0$	DCA2 Vertex $<$ 0.058	Decay Length $\times\sin\phi < 1.5$

Table 1 The K^0_S topological cuts parameters are shown on Table 1. Data from the author in this thesis.

II. K^0_S Reconstruction

After preparing for my analysis, I reconstruction K^0_S particles from pion pairs. The invariant mass of K^0_S with the topological cuts from Table 1 for all transverse momentum region is shown in Figure 18.

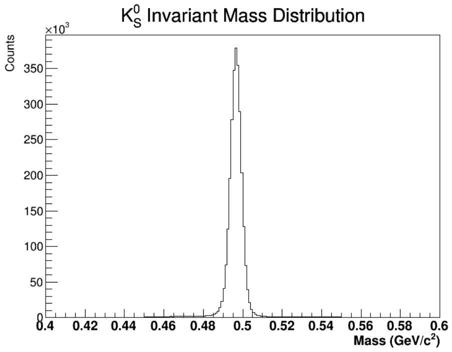

Fig. 18 Figure 18 shows the invariant mass of K_S^0 for all p_T for all centrality. The significance, defined by $S = \frac{Y}{\sqrt{Y+B}}$, is 13800 and the signal to background ratio is 8.98. Plot from the author in this thesis.

In particular, with HFT, we can still detect K_S^0 signal at very low transverse momentum region. The invariant mass of K_S^0 for $p_T < 0.3$GeV/c is presented in Figure 19.

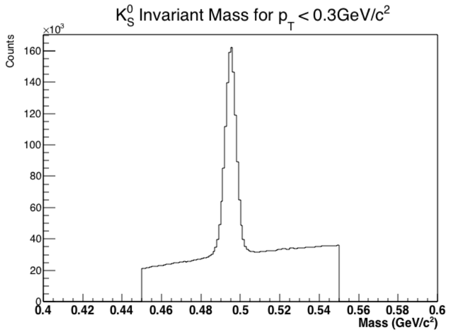

Fig. 19 Figure 19 shows the invariant mass of K_S^0 for $p_T < 0.3$GeV/c. The significance is approximately 3770 and the signal to background ratio is approximately 3.85. Plot from the author in this thesis.

The transverse momentum dependence of K_S^0 yield is shown in Figure 20.

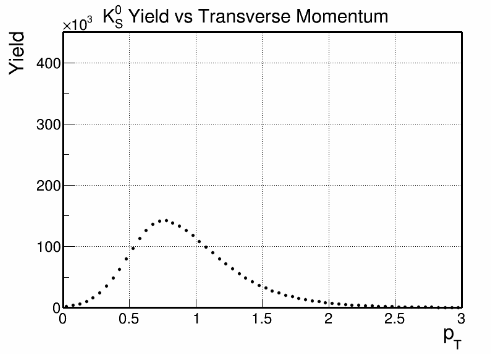

Fig. 20 The K_S^0 yield vs p_T is shown above. We can see that the curve of the yield goes to zero as $p_T \to 0$ and $p_T \to \infty$. Plot from the author in this thesis.

From Figure 20, we can see that the momentum distribution for $p_T > 0.2$GeV/c overall agrees with the thermal model predictions. Therefore, this verifies the statement that the systems created in relativistic heavy-ion collisions reach thermal equilibrium.

Figure 21 shows the plot of significance versus transverse momentum.

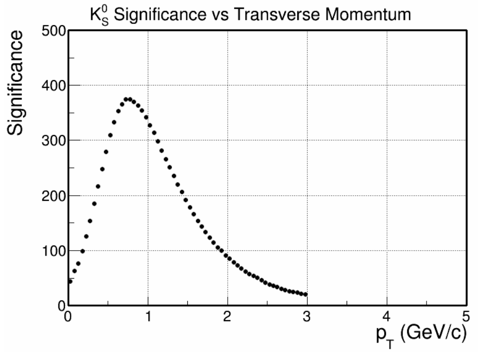

Fig. 21 Figure 21 shows the momentum dependence of significance. We can see for $p_T > 3\text{GeV/c}^2$, the significance is very low. The background plays a significant role for $p_T > 3$GeV/c. Plot from the author in this thesis.

Comparing Figure 21 with Figure 20, we can see that the significance distribution has similar shape to the momentum distribution. We know that in each p_T bin, the K_S^0 the yield Y is much greater background B ($Y >> B$). Therefore, the significance

$$S = \frac{Y}{\sqrt{Y+B}} \approx \frac{Y}{\sqrt{Y}} \approx \sqrt{Y} \tag{50}$$

Therefore, we can see that Figure 21 has similar shape to Figure 20 with different sizes.

III. Event Plane Reconstruction

The methods and related discussions of event plane reconstruction are presented in Chapter 1.5. For K_S^0 analysis, I choose the DCA to primary vertex to be less than 3cm and the transverse momentum to be greater than 0.1GeV/c and less than 2.0GeV/c. The pseudorapidity is greater than -1 and less than 1. Table 2 shows the cut parameter of event plane selection.

Event Plane Cut Parameters		
DCA < 0.3cm	0.1GeV/c < p_T < 2 GeV/c	-1 < η < -0.05 and 0.05 < η < 1

Table 2 The table above shows the cuts for event plane reconstruction. I make a 0.1 η gap in order to reduce short range correlations in small η range. Data from the author in this thesis.

I determine the angle ϕ of all particles from their momenta by tracing their helix tracks in the magnetic field. I recenter the event plane run by run and centrality by centrality. Since I use η sub-event method for my analysis [21], the recentering process is carried out in $\eta <$ 0 and $\eta > 0$ regions. The Ψ_2 distribution before recentering for $\eta > 0$, $\eta < 0$, and all η are presented in Figure 22, Figure 23, and Figure 24. Then, I fit the Ψ_2 distribution with a function $f(\Psi_2) = p_0 + p_1\cos(2\Psi_2 + p_2) + p_3\cos(4\Psi_2 + p_4) + p_5\cos(2\Psi_2 + p_6)$. The fitting parameter p_0 and p_1 are shown on Table 3.

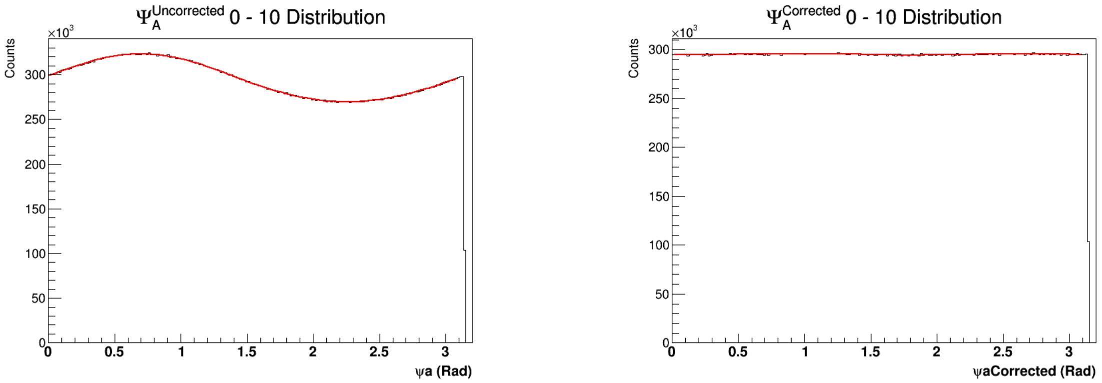

Fig. 22 The left plot shows the Ψ_2 distribution before recentering for all $\eta > 0$ in 0 - 10% centrality and the right plot shows the Ψ_2 distribution after recentering for $\eta > 0$ in 0 - 10% centrality. We can see that the recentering process makes the distribution much flatter. Plots from the author in this thesis.

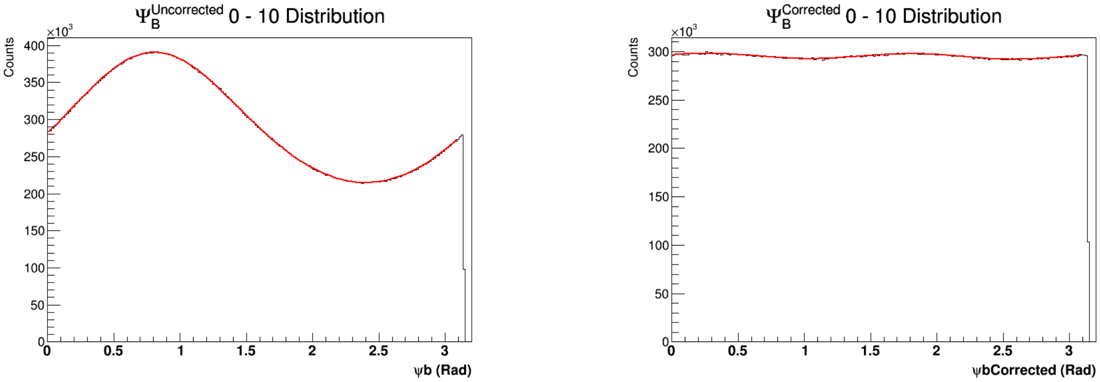

Fig. 23 The left plot shows the Ψ_2 distribution before recentering for $\eta < 0$ in 0 - 10% centrality and the right plot shows the Ψ_2 distribution after recentering for $\eta < 0$ in 0 - 10% centrality. We can see that the recentering process makes the distribution much flatter. Plots from the author in this thesis.

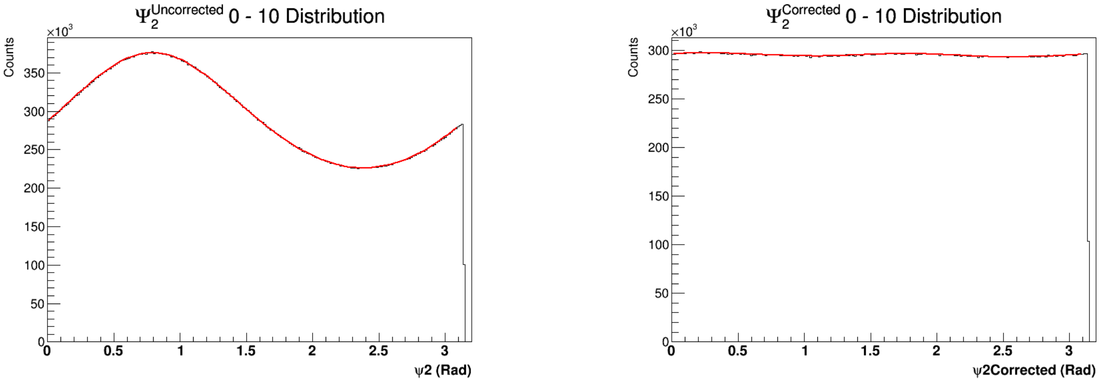

Fig. 24 The left plot shows the Ψ_2 distribution before recentering for all η in 0 - 10% centrality and the right plot shows the Ψ_2 distribution after recentering for all η in 0 - 10% centrality. We can see that the recentering process makes the distribution much flatter. Plots from the author in this thesis.

Fitting Parameters fot Ψ_2 Distribution						
Parameters	$\eta > 0$		$\eta < 0$		All η	
	Uncorrected	Corrected	Uncorrected	Corrected	Uncorrected	Corrected
p_0 $(\times 10^5)$	2.952	2.952	2.952	2.952	2.952	2.952
p_1 $(\times 10^{-4})$	-909 ± 2	-7 ± 2	-2950 ± 2	14 ± 2	-2520 ± 2	-22 ± 2

Table 3 The fitting parameter p_0 and p_1 for Ψ_2 distribution are presented in Table 3. Data from the author in this thesis.

The raw K_S^0 Yield vs centrality is shown in Figure 25

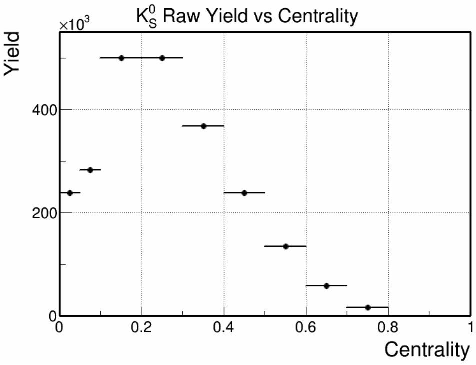

Fig. 25 The plot above is raw K_S^0 Yield vs Centrality. We can see that the yield is small in very central and peripheral centrality bins. The raw yield peaks around 20 - 30%. Plot from the author in this thesis.

IV. Resolution Calculation

The full event resolutions is calculated according to Equation (33) and Equation (34) in Chapter 1. The full event resolution in different centrality bins of the reconstructed event plane is shown on Table 4 and Figure 26.

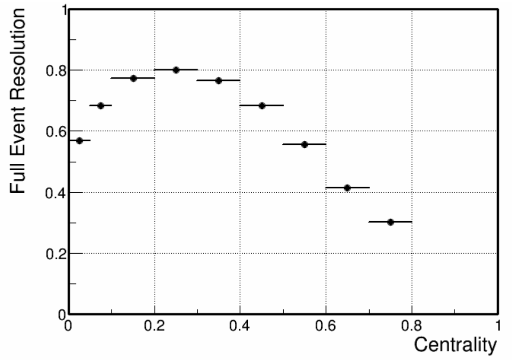

Fig. 26 The Full Event Resolution vs Centrality is shown above. The Resolution first increases as the centrality increases until it reaches the maximum about 0.80 in 20 - 30% and then decreases. It is consistent with Figure 25 because 20 - 30% centrality has the most counts. Plot from the author in this thesis.

Full Event Resolution vs Centrality									
Centrality	0 - 5%	5 - 10%	10 - 20%	20 - 30%	30 - 40%	40 - 50%	50 - 60%	60 - 70%	70 - 80%
Resolution	0.569	0.682	0.773	0.800	0.765	0.682	0.555	0.415	0.301

Table 4 The numerical values of the full event resolution of each centrality bin is shown in Table 4. Data from the author in this thesis.

As we can see from Figure 25 and Figure 26, both resolution and yield distribution have maximum around 20 - 30% centrality. Because I use the η subevent method to reduce short range correlations, the resolution should be the η subevent resolution, which is given by [21]

$$R_{sub} = \sqrt{\left\langle \cos[n(\Psi_n^a - \Psi_n^b)] \right\rangle} \tag{51}$$

The η subevent event resolution in different centrality bins of the reconstructed event plane is shown on Table 5 and Figure 27.

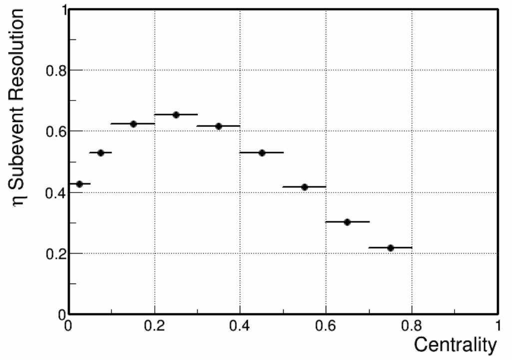

Fig. 27 The η Subevent Resolution vs Centrality is shown above. The Resolution first increases as the centrality increases until it reaches the maximum about 0.65 in 20 - 30% and then decreases. We also see that the η subevent resolution is always lower than the full event resolution because its statistics is lower. Plot from the author in this thesis.

η Subevent Resolution vs Centrality									
Centrality	0 - 5%	5 - 10%	10 - 20%	20 - 30%	30 - 40%	40 - 50%	50 - 60%	60 - 70%	70 - 80%
Resolution	0.427	0.529	0.624	0.654	0.615	0.530	0.416	0.302	0.216

Table 5 The numerical values of the η subevent resolution of each centrality bin is shown in Table 5. Data from the author in this thesis.

VI. Observed Elliptic Flow Measurement from K_S^0 $\Delta\phi$ Plot

As I discuss in Chapter 1 Equation (24), I can define $\Delta\phi = \phi - \Psi_2$. To calculate the elliptic flow from the K_S^0 $\Delta\phi$ distribution $\frac{dN(\Delta\phi)}{d\Delta\phi}$, I separate the K_S^0 invariant mass distribution into 12 $\Delta\phi$ bins for $0 < \Delta\phi < \pi$ and calculate the K_S^0 yield bin by bin. I extract v_2 values from fitting the Yield vs $\Delta\phi$ plot of each p_T bin by a function $f(\Delta\phi) = p_0[1 + v_2\cos(2\Delta\phi)]$. Examples of the fitting for Centrality 30 - 40% in 0.5GeV/c $< p_T <$ 0.6GeV, 0.6GeV/c $< p_T <$ 0.7GeV, and 0.7GeV/c $< p_T <$ 0.8GeV are shown in Figure 28.

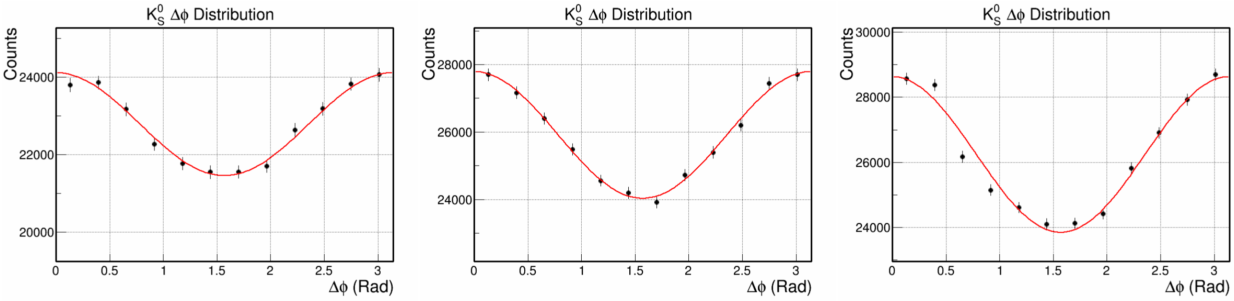

Fig. 28 The Yield vs $\Delta\phi$ plots and its optimal fits are shown above. In the left plot, the observed v_2 from the fit is $v_2^{obs} = 0.029 \pm 0.001$. In the middle plot, the observed v_2 from the fit is $v_2^{obs} = 0.036 \pm 0.001$. In the right plot, the observed v_2 from the fit is $v_2^{obs} = 0.045 \pm 0.001$. Plots from the author in this thesis.

As we can see from Figure 28, the Yield vs $\Delta\phi$ plots has a clear second order harmonics coefficients v_2, which demonstrate that the azimuthal anisotropic emissions of particles exist in heavy-ion collisions. This confirms the overlapping region where partons interact is indeed an almond shape.

VII. Elliptic Flow Measurement from K_S^0 after Resolution Correction

The actual elliptic flow v_2 is given by the resolution correction from the observed v_2 [21]

$$v_2 = \frac{v_2^{obs}}{R_{sub}} \tag{52}$$

The v_2 vs p_T for $\eta > 0$, $\eta < 0$, and all η plot is shown in Figure 29, Figure 30, and Figure 31

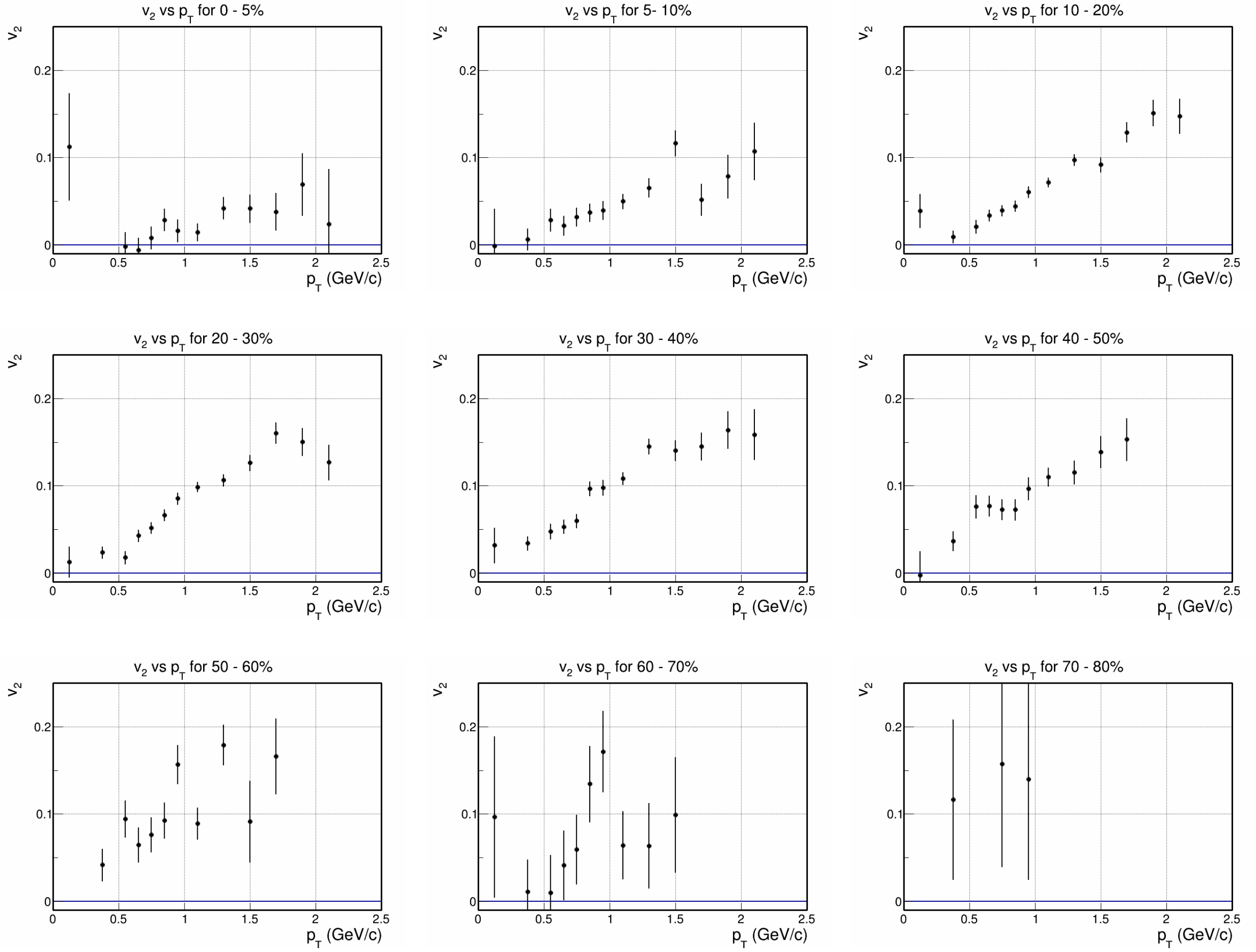

Fig. 29 The K_S^0 v_2 vs p_T plots for $\eta > 0$ plots for each centrality bin are shown above. Plots from the author in this thesis.

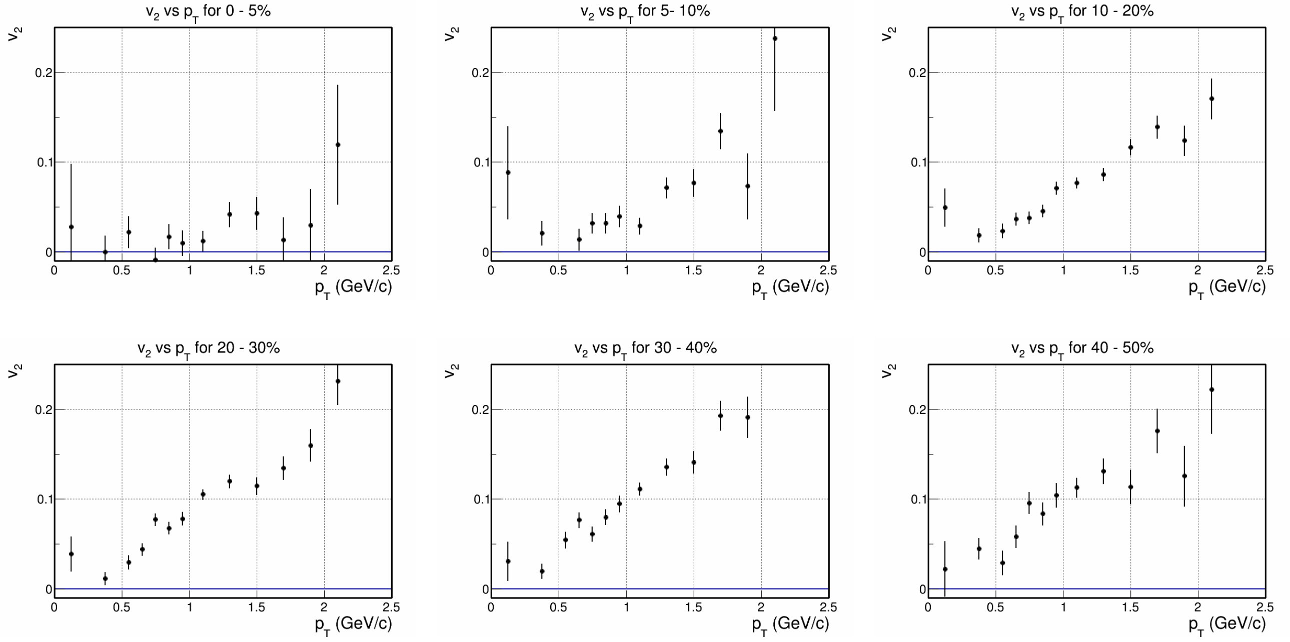

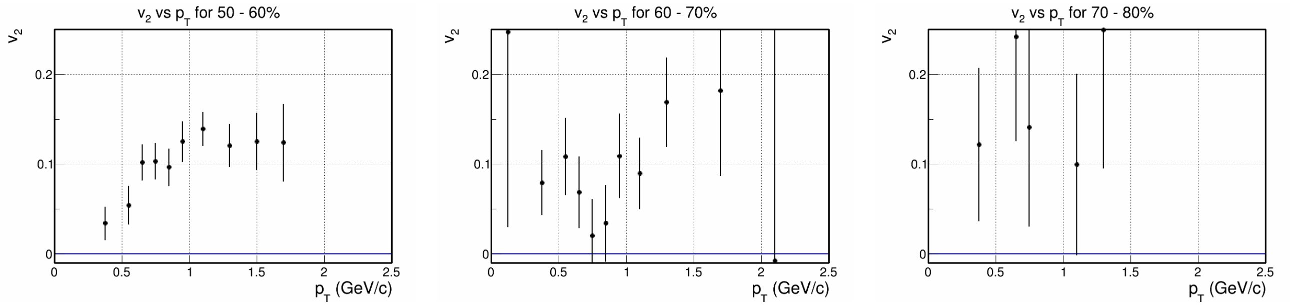
v2 vs pT for 50 - 60%
v2 vs pT for 60 - 70%
v2 vs pT for 70 - 80%

Fig. 30 The K_S^0 v_2 vs p_T plots for $\eta < 0$ plots for each centrality bin are shown above. Plots from the author in this thesis.

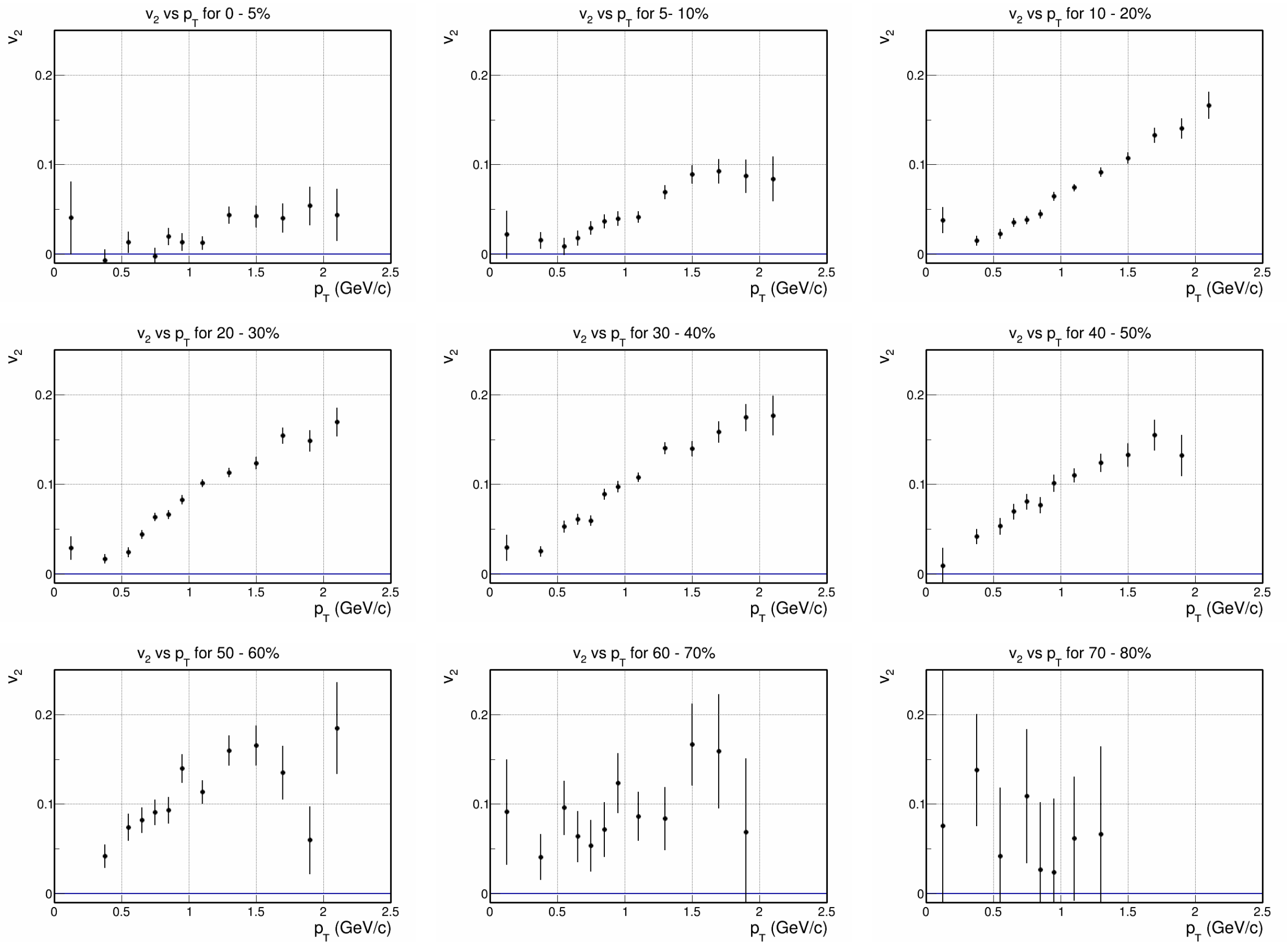
v2 vs pT for 0 - 5%
v2 vs pT for 5- 10%
v2 vs pT for 10 - 20%
v2 vs pT for 20 - 30%
v2 vs pT for 30 - 40%
v2 vs pT for 40 - 50%
v2 vs pT for 50 - 60%
v2 vs pT for 60 - 70%
v2 vs pT for 70 - 80%

Fig. 31 The K_S^0 v_2 vs p_T plots for all η for each centrality bin are shown above. Plots from the author in this thesis.

We can see that the K_S^0 vs v_2 in $\eta < 0$, $\eta > 0$, and all η are very similar to each other. The K_S^0 v_2 increases as p_T increases. In addition, K_S^0 v_2 are higher for peripheral collisions than central collisions.

VIII. Published K_S^0 Momentum Spectrum

The Published K_S^0 momentum spectrum for previous run with Au + Au at 200GeV is shown below [45]

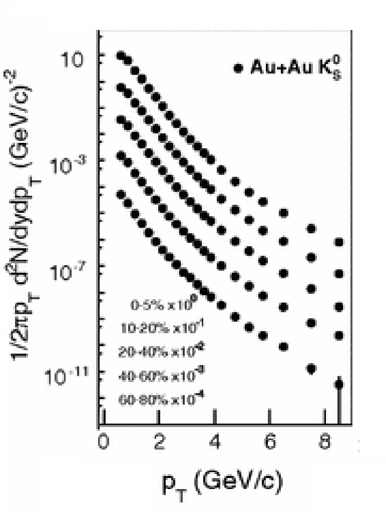

Fig. 32 The plot above shows K_S^0 Momentum Spectrum for centralities bins 0 - 5%, 10 - 20%, 20 - 40%, 40 - 60%, and 60 - 80%. The scale of the K_S^0 yield density $\frac{1}{2\pi p_T}\frac{d^2N}{dydp_T}$ is in log scale. The density of the centralities are scaled according to the legend in Figure 32. Plot from [45].

We notice that the published K_S^0 momentum spectrum for Au + Au at 200GeV obeys the thermal distribution $\frac{1}{2\pi p_T}\frac{d^2N}{dydp_T} = Ne^{\frac{\sqrt{p_T^2c^2+m^2c^4}}{k_BT}}$. If we fit the data points with exponential function and integrate for each centrality bins, we will get the theoretical yield of each centrality bin. Their ratio should be the same for all K_S^0 particles created in Au + Au collisions at 200GeV.

IX. K_S^0 Relative Yield Ratio in 0 - 80% Centrality Bins

As we can see from Figure 25, the yield of K_S^0 in centrality 0 - 10% is lower than 10 - 20%. This contradicts to our expectation. In the centrality 0 - 10%, there are more nucleons participate in the collisions than in 10 - 20%. The actual yield of K_S^0 should be higher. This is because different centralities have different efficiency. The efficiency is lower in 0 - 10% than 10 - 20%. The K_S^0 yield ratio of different centralities relative to the 0 - 5% centrality Bin is given by

$$\epsilon_i = \frac{Y_{P_i}}{Y_{P_1}} \tag{53}$$

The estimated relative K_S^0 yield ratio of each centrality bins from the K_S^0 momentum spectrum are shown on Table 6.

K_S^0 Relative Efficiency to Centrality Bin 0 - 5%					
Centrality	0 - 5%	10 - 20%	20 - 40%	40 - 60%	60 - 80%
Relative K_S^0 Yield Ratio	1	0.60 ± 0.06	0.37 ± 0.04	0.16 ± 0.02	0.058 ± 0.006

Table 6 The table shows the relative K_S^0 yield ratio of 0 - 5%, 10 - 20%, 20 - 40%, 40 - 60%, and 60 - 80% according to the K_S^0 momentum spectrum and Equation (53). Data from the author in this thesis.

Therefore, we multiply the yield of K_S^0 by the K_S^0 yield ratio of each centrality to get the actual yield of K_S^0 in experiment. The actual yield Y_i of K_S^0 is given by

$$Y_i = Y_1 \epsilon_i = \frac{Y_1 Y_{P_i}}{Y_{P_1}} \tag{54}$$

Or equivalently

$$\frac{Y_i}{Y_1} = \frac{Y_{P_i}}{Y_{P_1}} = const \tag{55}$$

Again, the ratio of the actual yield Y_i of K_S^0 in different centrality should be equal to the ratio of the theoretical yield in different centrality extracted from momentum spectrum. The distribution of the actual yield of each centrality after corrections is shown in Figure 33.

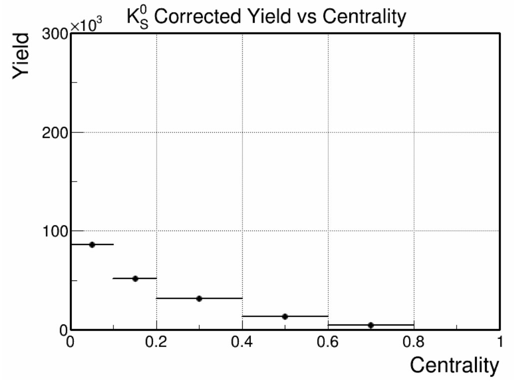

Fig. 33 The K_S^0 Actual Yield vs Centrality after efficiency corrected is shown in Figure 31. We can see that the most central bin 0 - 10% has the highest yield and the yield decreases as the collisions become more peripheral. Plot from the author in this thesis.

X. K_S^0 Elliptic Flow in 0 - 10% and 0 - 30% without Efficiency Correction

To combine centrality bins, we combine K_S^0 v_2 by weighting their actual yields Y

$$v_2 = \frac{\sum_i^N Y_i v_2^i}{\sum_i^N Y_i} \tag{56}$$

The corresponding propagated error is given by

$$\Delta v_2 = \frac{\sqrt{\sum_i^N (Y_i \Delta v_2^i)^2}}{\sum_i^N Y_i} \tag{57}$$

However, in this thesis, the precise values of K_S^0 spectrum is not available. Therefore, because I do not know exactly the efficiency of each centrality bin, I cannot combine different centrality bins by weighting their v_2. However, since the efficiency varies very little between 0 - 5% and 5 -10%. I can just treat them to have the same efficiency and combine their v_2 by weighting their raw K_S^0 yields. I also combine K_S^0 v_2 for 0 - 30% without efficiency correction. The plots for K_S^0 v_2 vs p_T in 0 - 10% and 0 - 30% are shown in Figure 34

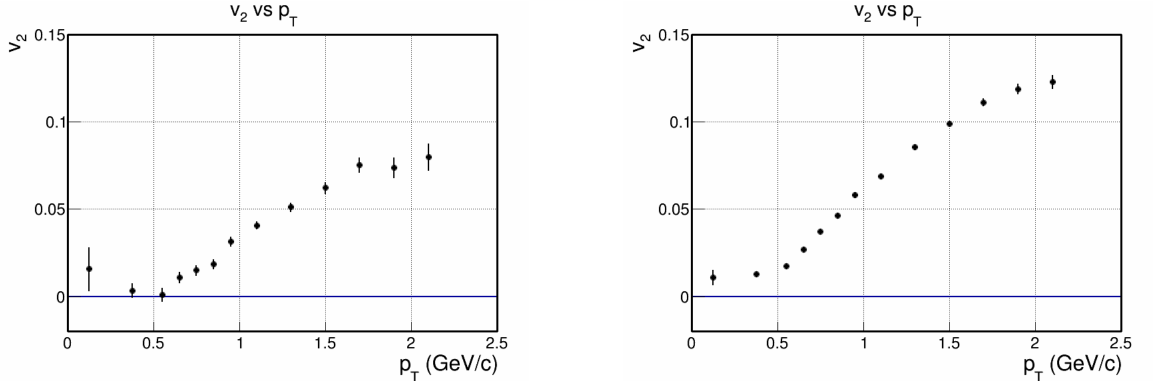

Fig. 34 The plots above show the weighted K_S^0 vs p_T in 0 - 10% and 0 - 30% centrality bins without efficiency correction. The left plot is for 0 - 10% and the right plot is for 0 - 30%. Plots from the author in this thesis.

XI. K_S^0 Average Elliptic Flow vs Centrality Bins

The average elliptic flow $\langle v_2 \rangle$ is defined by

$$\langle v_2 \rangle = \frac{\int_0^\infty v_2(p_T) \frac{dN}{dp_T} dp_T}{\int_0^\infty \frac{dN}{dp_T} dp_T} \tag{58}$$

The plot of K_S^0 Average Elliptic Flow $\langle v_2 \rangle$ vs Centrality Bins is shown below

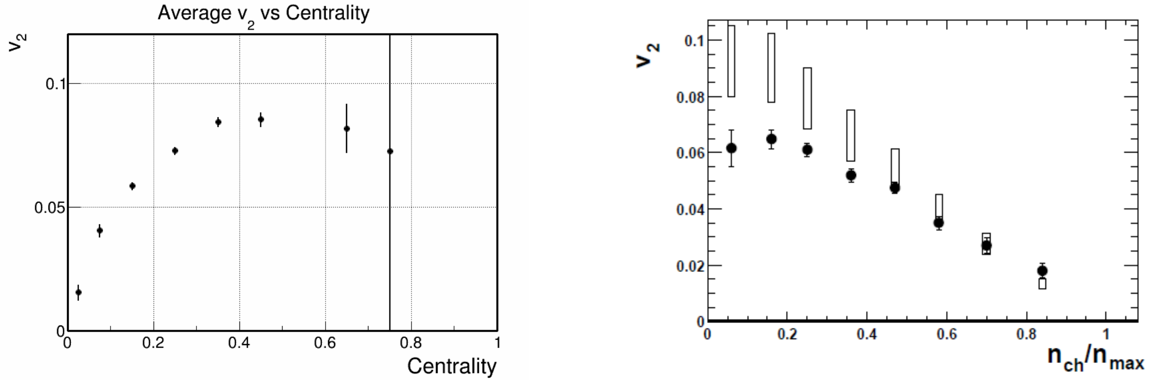

Fig. 35 The left plot shows the integrated K_S^0 $\langle v_2 \rangle$ vs Centrality. In the left plot, the $\langle v_2 \rangle$ is larger at peripheral collisions than central collisions. This is consistent with our expectation because peripheral collisions have larger eccentricity and thus should have larger $\langle v_2 \rangle$ given the relation that $v_2 \propto \epsilon$. The theoretical v_2 (open retangles) from the hydrodynamic limit and experimental v_2 (solid points) vs centrality is shown in the right plot [46]. Here, the larger the value n_{ch}/n_{max} is, the more central the collision is. The left plot is from the author in this thesis and the right plot is from [46].

As we can see in Figure 35, theoretical models predict that v_2 should increase about linearly as the centrality increases or n_{ch}/n_{max} decreases. However, we can see that when the centrality is greater than 40%, K_S^0 v_2 stops increasing. The probability of creating a quark-gluon plasma in high energy nuclear collision experiments is determined by the multiplicity and the collision energy. In the same collisions energy, for peripheral collisions, since the number of particles is smaller than the one in central collisions, the probability of creating quark-gluon plasma is smaller than central collisions. Because of the collectivity of quark-gluon plasma, the elliptic flow v_2 is greater when quark-gluon plasma is created. Therefore, as collisions get more peripheral, the elliptic flow v_2 stops increasing linearly, which contradicts to the predictions from theoretical calculations.

Chapter 3 Discussion and Summary

3.1. Comparison with Run 10 Data

Because I would like to focus on analyzing K_S^0 elliptic flow in the low transverse momentum region, I need to compare my analyses with published results and verify my analyses. I use my STAR Run 14 all η K_S^0 v_2 vs p_T to compare with the published STAR Run 10 K_S^0 v_2 results [47], which also use η subevent method, in centrality 0 - 10% and 0 - 30%. Table 7 shows the event selections for event plane reconstruction in Run 10 analyses. Figure 36 shows my analysis results with the published Run 10 results in 0 - 10% and 0 - 30%.

Run 10 Event Selections for Event Plane Reconstruction in Run 10 Analyses		
DCA < 0.3cm	0.15GeV/c < p_T < 2 GeV/c	-1 < η < -0.05 and 0.05 < η < 1

Table 7 The table above shows the cuts for event plane reconstruction. It is very similar to my cuts for event plane reconstruction from Table 2 except the lower bound of the transverse momentum p_T > 0.15GeV/c instead of p_T > 0.10GeV/c. Data from [48].

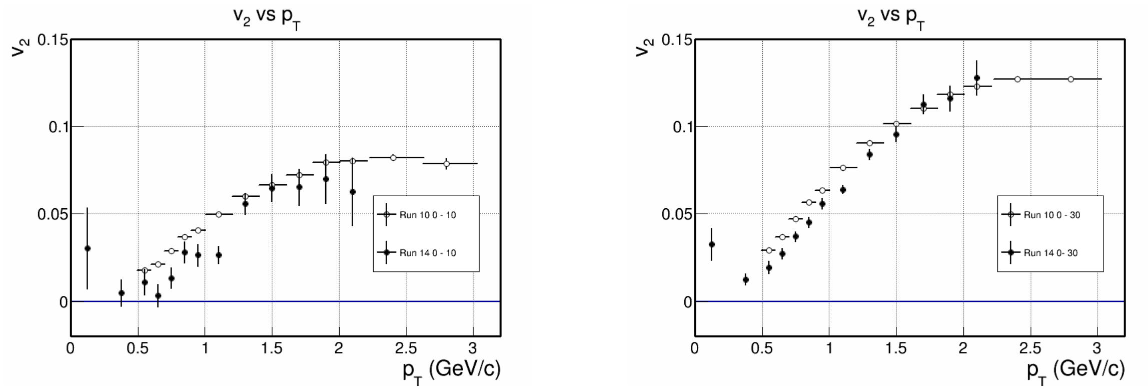

Fig. 36 The open circles are the Run 10 results without HFT and the black circles are my Run 14 results with HFT from my analyses in 0 - 10% centrality. The left plot shows the K_S^0 v_2 vs p_T in 0 - 10% and the right plot shows K_S^0 v_2 vs p_T in 0 - 30%. Plots from the author in this thesis and from [47].

From Figure 36, we can see that my K_S^0 v_2 vs p_T for 0 - 10% and 0 - 30% are consistent with the published Run 10 results for p_T > 1.5GeV/c and are systematically lower than the published Run 10 results for p_T < 1.5GeV/c.

3.2. Discussion about My Analysis

From Figure 36, we can see that my preliminary results in 0 - 10% and 0 - 30% are consistent within statistical error for p_T >1.5GeV/c and systematically lower than the Run 10 results for p_T < 1.5GeV/c. Possible reasons for the inconsistency of my analysis with the Run 10 results are the systematic errors in our calculations, the efficiency weighting in 0 - 10% and 0 - 30%, and the errors on Run 14 production.

In Run 10 analysis, K_S^0 v_2 results are only presented in 0 - 10% and 0 - 30% instead of the standard 9 centrality bins. In addition, the Run 10 author only provides me with the preliminary results, which does not include systematic error. Therefore, it is hard to find out why my result does not agree with it. In addition, the resolution distribution and the actual yield of K_S^0 for all centrality bins in Run 10 are not available. To obtain the efficiency, we estimate the K_S^0 yield of all centrality bins from the published momentum spectrum. Our calculations are limited by the available centrality bins in the publish results, which are 0 - 5%, 10 - 20%. 20 - 40 %, 40 - 60%, and 60 - 80%. This makes it very difficult to compare our results and find out the errors in my analyses.

Finally, some errors in the Run 14 production data are recently found. This may also be a reason why my result K_S^0 v_2 vs p_T is inconsistent with the published result for $p_T < 1.5$ GeV/c. After we fix these errors, I will do my analysis again and compare the result with the published Run 10 results.

In the next sections, I will investigate the effects of the η gap on event plane reconstruction and the number-of-constituent quark equation fit from quark-coalescence model [49] on K_S^0 v_2 in 0 - 30% and 0 - 80%.

3.3 The Effects of η Gap on K_S^0 v_2

In event plane reconstruction, non-flow correlations, for instance, the back-to-back jets created from heavy-ion collisions, may affect K_S^0 v_2 [50]. To reduce this non-flow effect, we choose an η gap to reject the back-to-back jets in our event plane reconstruction. However, we cannot choose the η gap too large because it will significantly lower our statistics for event plane reconstruction. Figure 37 shows K_S^0 v_2 vs p_T in 30 - 40% centrality plots for 0.10 and 0.20 η gap.

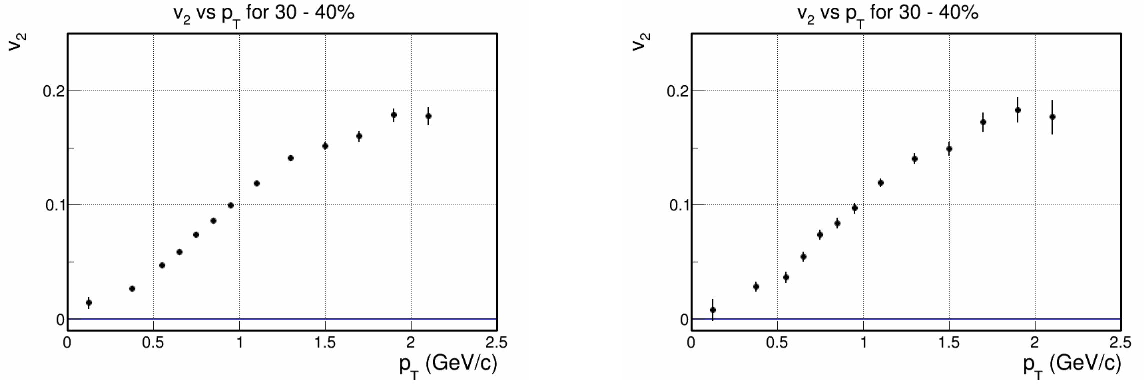

Fig. 37 The plots above show the K_S^0 v_2 vs p_T in 30 - 40% centrality plots for 0.10 and 0.20 η gap. The left plot shows for 0.10 η gap and the right plot is for 0.20 η gap. Plots from the author in this thesis.

From Figure 37, we can see that the results with different η are statistically consistent. We may estimate the systematic error from choosing different η gaps to calculate K_S^0 v_2.

3.4. The Quark-Coalescence Model and K_S^0 v_2 in 0 - 30% and 0 - 80%

The quark content of K_S^0 is

$$\left|K_S^0\right\rangle = \frac{\left|d\bar{s}\right\rangle + \left|s\bar{d}\right\rangle}{\sqrt{2}} \tag{59}$$

It is a meson and thus consists of one quark and one antiquark. According to the number-of-constituent-quark (NCQ) scaling law from quark-coalescence model [49]

$$v_2(n) = \frac{an}{1 + e^{-\frac{\frac{p_T}{n} - b}{c}}} - dn \tag{60}$$

Here, n is the number of quarks inside the hadron. The parameters a, b, c, and d are constant for all hadrons. Their values are presented in Table 8 on the row of published results. For K^0_S, theoretically, we expect that n should be equal to 2.

According to the reference [49], the author fits the v_2 vs p_T plots for all p_T. In my analysis, I will fit my K^0_S v_2 vs p_T in 0 - 30% and 0 - 80% with all p_T and 0.2GeV/c $< p_T <$ 2.1 GeV/c. I fix the parameter $c = 0.2$ and fit the K^0_S v_2 vs p_T plot. Here are my fitting results

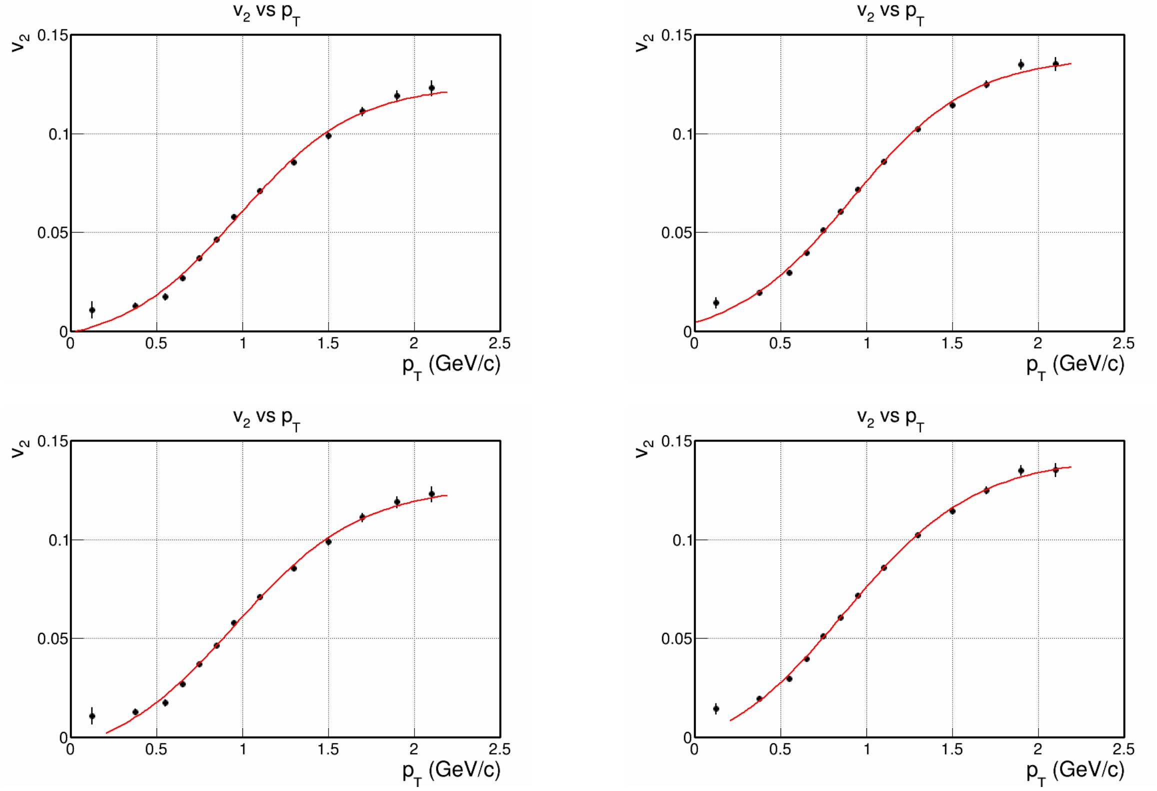

Fig. 38 The plots above show the K^0_S elliptic flow v_2 vs transverse momentum p_T in 0 - 30% and 0 - 80% (no efficiency corrections) with the corresponding NCQ fit functions. I fit the Equation (60) with my plots. The upper left plot is for K^0_S v_2 vs p_T in 0 - 30% with all p_T fit. The upper right plot is for K^0_S v_2 vs p_T in 0 - 80% with all p_T fit. In the lower plot, I exclude the lowest p_T data point and perform fitting because the lowest p_T data point deviates from the fits. The lower left plot is for K^0_S v_2 vs p_T in 0 - 30% with 0.2GeV/c $< p_T <$ 2.1GeV/c fit. The lower right plot is for K^0_S v_2 vs p_T in 0 - 80% with 0.2GeV/c $< p_T <$ 2.1GeV/c fit. The results of fitting parameters and the published results [48, 50] are shown in Table 8. Plots from the author in this thesis.

Fitting Parameters for NCQ Scaling Equation from Quark-Coalescent Model						
Parameters	n	a	b	c	d	χ^2/ndf
Upper Left Plot	1.70 ± 0.13	0.077 ± 0.002	0.57 ± 0.05	0.20	0.005 ± 0.002	2.66
Upper Right Plot	1.73 ± 0.10	0.083 ± 0.002	0.53 ± 0.04	0.20	0.003 ± 0.002	1.95
Lower Left Plot	**1.85 ± 0.17**	0.077 ± 0.002	0.52 ± 0.05	0.20	0.008 ± 0.003	2.25
Lower Right Plot	**1.91 ± 0.14**	0.082 ± 0.002	0.46 ± 0.05	0.20	0.007 ± 0.003	1.18
Published Values	2.3 ± 0.4	0.1	0.35	0.2	0.03	N/A

Table 8 The fitting parameters are for NCQ scaling equation for K_S^0 v_2 vs p_T plot is shown above. Data from row 1 to row 5 is from the author in this thesis. The data in the last row are from [49] and [51].

The K_S^0 v_2 vs p_T in 0 - 30% and 0 - 80% agree with the number-of-constituent-quark (NCQ) scaling law from quark-coalescence model [49] according to the Figure 38 and Table 8. **The number of quark n for the lower plots are consistent with the published values and the theoretical predictions within statistical error from the NCQ equation fitting.**

Chapter 4 Conclusion

4.1 Summary

In this thesis, I have introduced high energy nuclear physics, explained the physics motivations of elliptic flow analysis of K_S^0 in heavy-ion collision experiments, carried out my preliminary analyses on K_S^0 elliptic flow for 466 million events from STAR Run 14 Au + Au collisions at $\sqrt{s_{NN}} = 200\text{GeV}$ data with the upgraded Heavy Flavor Tracker detector, and compared my analyses with the published Run 10 results.

First, I reconstruct K_S^0 particles from pion pairs in the decay channel $K_S^0 \rightarrow \pi^+ + \pi^-$ with track selections and event selections. To get a higher K_S^0 significance for my analysis, I study five parameters of pion tracks DCA1, DCA2, DCA Daughters, $\cos\theta$, and DCA2 Vertex defined by Figure 17. The topological cuts values are presented in Table 1.

Then, after reconstructing K_S^0 from pion pairs, I show the K_S^0 invariant mass distribution in Figure 18 and the yield of K_S^0 vs transverse momentum p_T in Figure 19. The invariant mass is $m = (0.497 \pm 0.001)\text{GeV/c}^2$ and agrees with the published K_S^0 results. Technically, the dynamical properties such as the pseudo-rapidity η, the transverse momentum p_T, and the azimuthal angle ϕ of all K_S^0 particles reconstructed from pion pairs are recorded and stored.

Subsequently, I use η subevent method to calculate K_S^0 v_2 vs p_T. I first select the tracks for event plane reconstruction. The track selections are presented in Table 2. Then, I use the tracks to calculate the Q-Vectors of the event plane and recenter the event plane for each run and each centrality bin. The detail calculations are show in section 1.5. Figure 22, Figure 23, and Figure 24 show the Ψ_2 distribution for $\eta < 0$, $\eta > 0$, and all η before recentering and after recentering respectfully. We can see that the event plane is much flatter after recentering.

Moreover, I calculate the event plane resolutions for each centrality bin using η subevent method. The full event resolution and η subevent resolution are shown in Figure 26 and Figure 27. In order to reduce the non-flow correlation, I choose a 0.1 η gap and use the η subevent method. Therefore, I use the η subevent resolution in my analysis for the calculations of K_S^0 elliptic flow v_2.

Next, I extract the observed K_S^0 v_2 from fitting the yield distribution of 12 $\Delta\phi$ bins for each p_T bins with a sinusoidal function $f(\Delta\phi) = N[1 + v_2\cos(2\Delta\phi)]$ in each centrality bin. As shown in Figure 28, azimuthal anisotropy for K_S^0 is observed in Au + Au collisions at $\sqrt{s_{NN}} = 200\text{GeV}$, confirming that the overlapping reaction region is an almond shape. The actual v_2 is then corrected by the resolution. K_S^0 v_2 vs p_T in each centrality for all η are presented in Figure 30 and the average elliptic flow $\langle v_2 \rangle$ vs centrality is presented in Figure 35.

In addition, to study the K_S^0 yield vs centrality, I use the K_S^0 momentum spectrum and my raw yield in each centrality bins to calculate the relative K_S^0 ratio of each centrality bin. The detail calculations are shown in section 3.2.IX and the K_S^0 Yield vs Centrality is shown in Figure 31.

Finally, I combine the 0 - 10% and 0 - 30% v_2 vs p_T plot and compare it with the published Run 10 results. My results are consistent with the published data for $p_T > 1.5\text{GeV/c}$ and systematically lower than the published results for $p_T < 1.5\text{GeV/c}$. I propose several possible reasons. It may be due to the systematic error and the unavailability of Run 14 K_S^0 momentum spectrum. I also study the effects of η gap and use the number-of-quark-constituent equation from quark-coalescence model to fit my K_S^0 v_2 vs p_T in 0 - 30% and 0 - 80% plots. I find that overall, my fitting results agree with the published values.

In conclusion, our $\mathbf{K_S^0}$ $\mathbf{v_2}$ results are consistent with the quark coalescence fit. This implies that quark-gluon plasma is formed in Au+Au collisions at $\sqrt{s_{NN}} = 200\,GeV$ and hadrons are formed at the later phase of quark-gluon plasma via the coalescence process. The collectivity observed in the final hadrons, including the $\mathbf{K_S^0}$, are indeed created in the early partonic quark-gluon plasma phase.

4.2 Future Analyses

Because of the limited time, I have only completed my preliminary K_S^0 v_2 analysis, which is not fully consistent with the published results. In the future, I will look into different centrality bins like 10 - 40% and 20 - 60% and get a better efficiency correction from the Run 14 K_S^0 momentum spectrum for all centrality bins. I also plan to carry out v_2 analyses for charged hadrons such as π^+, π^-, K^+, and K^- as a cross check of my analyses. I expect the K^+ and K^- v_2 to be consistent with my K_S^0 v_2.

Because the low p_T data are not available prior to the HFT detector [41], I will focus on analyzing the K_S^0 v_2 at low p_T and carry out analysis on K_S^0 transverse momentum spectrum. In order to complete the analysis, I will analyze the K_S^0 momentum spectrum and extract the detecting efficiency via the established embedding method in STAR experiment. These results will not only be important for the azimuthal analysis but also important for extract collectivity parameters in the future. Moreover, I will conduct a comprehensive evaluation on the systematic error of K_S^0 v_2 in my analyses. Finally, I will preform Blast-Wave thermal model fit to the experimental data to investigate the collectivity of the bulk quark-gluon plasma medium to decipher the properties of quark-gluon plasma. My analyses of K_S^0 may be published in a peer-reviewed journal in the future.

Reference

[1] M. Peskin and D. Schroeder, An Introduction to Quantum Field Theory, Westview, 1995

[2] D. Griffiths, Introduction to Elementary Particles, 2nd ed, Wiley-VCH, 2008

[3] F. Wilczek. Nature 391 330-331 (1998)

[4] J. Adams. el al. (STAR Collaboration) Nucl. Phys. A 757 102-183 (2005)

[5] F. Chen, Introduction to Plasma Physics and Controlled Fusion, Plenum Press, New York and London, 1974

[6] B. Muller Rept. Prog. Phys. 58 611-636 (1995)

[7] M. Anderson. et al. (STAR Collaboration) Nucl. Instrum. Meth. A 499 (2003) 659-678

[8] B. V. Jacak and B. Muller. Science. 337 (2012) 310-314

[9] L. Kumar. Mod. Phys. Lett. A, 28 1330033 (2013)

[10] E. Laermann and O. Philipsen, Annu. Rev. Nucl. Part. Sci. 53 (2003) 163

[11] Z. Fodor, S.D. Katz, JHEP 0404 (2004) 050

[12] S. Gupta, X. Luo, B. Mohanty, H. G. Ritter, and N. Xu. Science 332 (2011) 1525-1528

[13] T. Nayak Pramana 79 (2012) 719-735

[14] L. Pang, Q. Wang, and X. Wang, Phys. Rev. C 86, 024911 (2012)

[15] A. Chodos, R. L. Jaffe, K. Johnson, C. B. Thorn, and V. F. Weisskopf, Phys. Rev. D 9, 3471 (1974)

[16] C. Misner, K. Thorne, and J. Wheeler, Gravitation, W. H. Freeman and Company, San Francisco, 1973

[17] Learning about Electronics, http://www.learningaboutelectronics.com/Articles/Cartesian-rectangular-to-spherical-coordinate-converter-calculator.php, Website

[18] S. Voloshin and Y. Zhang. Z. Phys. C 70 (1996) 665-672

[19] L. Olsson, Dihadron Correlations and Flow, Phd Thesis for Lund University, 2013

[20] S. Chatrchyan et al. (CMS Collaboration) Eur. Phys. J. C74 (2014)

[21] A. M. Poskanzer and S. A. Voloshin, Phys. Rev. C 58, 1671 (1998)

[22] S. A. Voloshin, A. M. Poskanzer, A. Tang and G. Wang, Phys. Lett. B 659 (2008) 537.

[23] J. Ollitrault, A. M. Poskanzer, and S. A. Voloshin, Phys. Rev. C 80, 014904 (2009)

[24] G. S. Denicol, T. Kodama, and T. Koide. J. Phys. G 37, 094040 (2010)

[25] D. Molnar and S. A. Voloshin, Phys. Rev. Lett. 91, 092301 (2003)

[26] STAR Collaboration, https://www.star.bnl.gov/public/tpc/notebooks/StarCDR.pdf, Website

[27] K. H. Ackermann. et al. Nucl. Instrum. Meth. A 499 (2003) 624-632

[28] D. d'Enterria, Quantum Chromo Many-body Dynamics Probed in the Hard sector at RHIC, 39th Rencontres de Moriond on QCD and High-Energy Hadronic Interactions, 2004

[29] The PHENIX Collaboration, http://www.phenix.bnl.gov, Website

[30] Adcox, K. et al. (PHINEX Collaboration) Nucl. Instrum. Meth. A 499 (2003) 469-479

[31] ALICE Collaboration, http://alice-collaboration.web.cern.ch, Website

[32] Alme. J. et al. (ALICE Collaboration) Nucl. Instrum. Meth. A 622 (2010) 316-367

[33] ALICE Photos Web page, http://epweb2.ph.bham.ac.uk/user/evans/lead2010/Picture1.jpg, Website

[34] CMS Collaboration, http://cms.web.cern.ch, Website

[35] CMS Detector Design, http://cms.web.cern.ch/news/cms-detector-design, Website

[36] ATLAS Collaboration, https://atlas.web.cern.ch/Atlas/Collaboration/, Website

[37] The ATLAS Experiment, http://hedberg.web.cern.ch/hedberg/home/atlas/atlas.html, Website

[38] C. Lippmann. Nucl. Instrum. Mech A 666 (2012) 148-172

[39] J. Schambach. et al. (STAR Collaboration) Int. J. Mod. Phys. E16 (2007) 2496-2502

[40] W. J. Llope. Nucl. Instrum. Meth. A 661 (2012) 110-113

[41] C. Chasman et al. (STAR Collaboration), A Heavy Flavor Tracker for STAR, 2008, LBNL/PUB-5509-2008.

[42] G. Contin, The STAR Heavy Flavor Tracker (HFT) and Upgrade Plan, Quark Matter 2015, Presentation

[43] C. Adler. et al. (STAR Collaboration) Phys. Rev. C 66, 034904 (2002)

[44] K.A. Olive. et al. (Particle Data Group) Chin. Phys. C, 38, 090001 (2014)

[45] G. Agakishiev. et al. (STAR Collaboration) Phys. Rev. Lett. 108, 072301 (2012)

[46] K. H. Ackermann. et al. (STAR Collaboration) Phys. Rev. Lett. 86, 402 (2001)

[47] L. Adamczyk. el al. (STAR Collaboration) Phys. Rev. Lett. 116, 062301 (2016)

[48] H. Masui, B. Mohanty, Md. Nasim, S. Shi, and X. Sun, Centrality Dependence of Multi-strange Hadron v2 in Au+Au Collisions at 200 GeV, Analysis Notes

[49] X. Dong, S. Esumi, P. Sorensen, N. Xu , and Z. Xu, Phys. Lett. B597, 328(2004)

[50] B. Alver. et al. (PHOBOS Collaboration) Phys. Rev. C 81, 034915 (2010)

[51] B. I. Abelev. et al. (STAR Collaboration) Phys. Rev. Lett. 99, 112301 (2007)